1   **Low Cobalt Inventories in the Amundsen and Ross Seas Driven by High Demand for**
2   **Labile Cobalt Uptake Among Native Phytoplankton Communities**

3   **Rebecca J. Chmiel[1,2], Riss M. Kellogg[1,2], Deepa Rao[1,2], Dawn M. Moran[2], Giacomo R.**
4   **DiTullio[3], and Mak A. Saito[2]**

5   [1] MIT/WHOI Joint Program in Oceanography/Applied Ocean Science and Engineering, Woods
6   Hole, MA, 02543, USA

7   [2] Department of Marine Chemistry and Geochemistry, Woods Hole Oceanographic Institution,
8   Woods Hole, MA, 02543, USA

9   [3] Hollings Marine Laboratory, 331 Fort Johnson, Charleston SC, 29412, USA

11   Corresponding author: Mak Saito (msaito@whoi.edu)

12   **Key Points:**

13   - A significantly smaller dCo inventory was observed in the Ross Sea during the
14   2017/2018 austral summer compared to two expeditions in 2005/2006.

15   - The drawdown of the labile dCo fraction can be explained by higher rates of Co uptake
16   by phytoplankton.

17   - This change may be due to the alleviation of Fe limitation through inputs from increased
18   glacial melting and subsequent development of intermittent vitamin B_{12} and/or Zn
19   limitation, both of which would be expected to increase the demand for Co among
20   plankton communities.

Abstract

Cobalt (Co) is a scarce but essential micronutrient for marine plankton in the Southern Ocean and coastal Antarctic seas where dissolved cobalt (dCo) concentrations can be extremely low. This study presents total dCo and labile dCo distributions measured via shipboard voltammetry in the Amundsen Sea, Ross Sea and Terra Nova Bay during the CICLOPS (Cobalamin and Iron Co-Limitation of Phytoplankton Species) expedition. A significantly smaller dCo inventory was observed during the 2017/2018 CICLOPS expedition compared to two 2005/2006 expeditions to the Ross Sea conducted over a decade earlier. The dCo inventory loss (~10–20 pM) was present in both the surface and deep ocean and was attributed to the loss of labile dCo, resulting in the near-complete complexation of dCo by strong ligands in the photic zone. A changing dCo inventory in Antarctic coastal seas could be driven by the alleviation of iron (Fe) limitation in coastal areas where the flux of Fe-rich sediments from melting ice shelves and deep sediment resuspension may have shifted the region towards vitamin B_{12} and/or zinc (Zn) limitation, both of which are likely to increase the demand for Co among marine plankton. High demand for Zn by phytoplankton can result in increased Co and cadmium (Cd) uptake because these metals often share the same metal uptake transporters. This study compared the magnitudes and ratios of Zn, Cd and Co uptake (ρ) across upper ocean profiles and observed order of magnitude uptake trends ($\rho Zn > \rho Cd > \rho Co$) that paralleled the trace metal concentrations in seawater. High rates of Co and Zn uptake were observed throughout the region, and the speciation of available Co and Zn appeared to influence trends in dissolved metal : phosphate stoichiometry and uptake rates over depth. Multi-year loss of the dCo inventory throughout the water column may be explained by an increase in Co uptake into particulate organic matter and subsequently increased flux of Co into sediments via sinking and burial. This perturbation of the Southern Ocean Co biogeochemical cycle could signal changes in the nutrient limitation regimes, phytoplankton bloom composition, and carbon sequestration sink of the Southern Ocean.

Plain Language Summary

Cobalt is an important micronutrient for plankton, yet is often scarce throughout the oceans. A 2017/2018 expedition to coastal Antarctica, including regions of the Amundsen Sea and the Ross Sea, discovered lower concentrations of cobalt compared to two past expeditions in 2005 and 2006. In particular, this expedition observed lower concentrations of deep-ocean labile cobalt, or "free" cobalt unbound to strong organic molecules, the type of cobalt preferred by phytoplankton for uptake as a micronutrient. It is possible that a shifting nutrient landscape due to changing inputs of other micronutrients like dissolved iron is causing the lower dissolved cobalt concentrations, and may also be affecting the demand for micronutrients like dissolved zinc and vitamin B_{12}, which contains a cobalt atom. We have modeled how increased cobalt uptake by plankton can result in the lower deep cobalt concentrations over a time period of 12 years.

1 Introduction

Coastal Antarctic seas are highly productive environments for phytoplankton blooms and are characterized by high nutrient, low chlorophyll (HNLC) surface waters that tend to be growth limited by iron (Fe) and other trace metal micronutrients (Martin et al., 1990; Arrigo et al., 2008, 2012). During the spring and summer months, katabatic winds and fragmenting sea ice form open coastal polynyas in the Amundsen and Ross Seas that host high phytoplankton productivity and act as significant global carbon sinks (Arrigo et al., 2012). In the winter, ice cover supports the

64 turnover of deep waters that allow trace metals like Fe to be redistributed to the upper ocean
65 (Sedwick and DiTullio, 1997; Sedwick et al., 2011). Phytoplankton blooms in coastal Antarctic
66 polynyas are dominated by eukaryotes such as diatoms and the haptophyte *Phaeocystis antarctica*
67 (Arrigo et al., 1999; DiTullio et al., 2003), while cyanobacteria like *Prochlorococcus* and
68 *Synechococcus*, which are highly abundant in the adjacent South Pacific and South Atlantic gyres,
69 are near-absent from the phytoplankton community in the Southern Ocean (DiTullio et al., 2003;
70 Bertrand et al., 2011; Chandler et al., 2016).

71 Cobalt (Co) is an essential trace metal nutrient for many marine plankton and is relatively
72 scarce in the marine environment, often present in the dissolved phase (dCo) in picomolar
73 concentrations (10^{-12} mol L^{-1}). Co acts as a cofactor for metalloenzymes like carbonic anhydrase,
74 a crucial enzyme in the carbon concentrating mechanism of photosynthetic phytoplankton (Sunda
75 and Huntsman, 1995; Roberts et al., 1997; Kellogg et al., 2020), and vitamin B$_{12}$ (cobalamin),
76 which can be used for the biosynthesis of methionine but is only produced by some bacteria and
77 archaea (Warren et al., 2002; Bertrand et al., 2013). In the Ross Sea, vitamin B$_{12}$ availability has
78 been observed to co-limit phytoplankton growth with iron (Fe) when bacterial abundance is low
79 (Bertrand et al., 2007). Some phytoplankton exhibit flexible vitamin B$_{12}$ metabolisms and can
80 express a vitamin B$_{12}$-independent methionine synthase pathway (*metE* gene) instead of the
81 vitamin B$_{12}$-dependent pathway (*metH* gene), allowing these organisms to thrive in vitamin-
82 depleted environments (Rodionov et al., 2003; Bertrand et al., 2013; Helliwell, 2017). Recently,
83 *P. antarctica* was discovered to contain both *metH* and a putative *metE* gene, displaying a
84 metabolism that is flexible to vitamin B$_{12}$ availability (Rao et al., [In review]). Additionally, recent
85 observations of Zn co-limitation with Fe have been documented in the Ross Sea (Kellogg et al.,
86 [Submitted]), suggesting a complex landscape of trace metal and vitamin stress interactions in the
87 otherwise macronutrient-rich waters of coastal Antarctica.

88 Dissolved Co is present as two primary species in the marine environment: a "free" labile
89 Co(II) species with weakly bound ligands and a Co(III) species that is strongly bound to organic
90 ligands (K$_s$ > $10^{16.8}$) (Saito et al., 2005). Labile dCo is considered to be more bioavailable to marine
91 microbes than strongly-bound dCo, although there is evidence that phytoplankton communities
92 can access Co in strongly-bound organic ligand complexes (Saito and Moffett 2001) and that
93 microbial communities may produce extracellular Co ligands that stabilize dCo and prevent its
94 loss via scavenging to manganese (Mn)-oxide particles (Saito et al., 2005; Bown et al., 2012).
95 Previous dCo sampling expeditions to the Ross Sea, including two 2005/2006 Controls of Ross
96 Sea Algal Community Structure (CORSACS) expeditions (Saito et al., 2010) and fieldwork in
97 2009 that sampled the water column below early spring sea ice in the McMurdo Sound (Noble et
98 al., 2013), reported relatively high concentrations of labile dCo in the surface Ross Sea when
99 compared to the tropical and subtropical global oceans, suggesting that labile dCo was fairly
100 replete and bioavailable to phytoplankton at the time (Saito et al., 2010).

101 This study examines the biogeochemical cycle of Co in the Amundsen and Ross Seas
102 during the 2017/2018 austral summer as part of the Cobalamin and Iron Co-Limitation of
103 Phytoplankton Species (CICLOPS) expedition. Here, we present profiles of dCo speciation that
104 revealed a lower dCo inventory during the 2017/2018 summer bloom compared to that observed
105 during the 2005/2006 CORSACS expeditions, as well as mostly undetectable concentrations of
106 labile dCo in the surface ocean. Additional datasets of dissolved zinc (dZn) and cadmium (dCd),
107 as well as profiles of Co, Zn and Cd uptake rates measured by isotope tracer incubation
108 experiments suggest that regions of vitamin B$_{12}$ and Zn stress within phytoplankton blooms could

109 be driving high demand for bioavailable Co in the surface ocean. The results presented by this
110 study reveal a substantial perturbation of the Co cycle, a shift towards vitamin B$_{12}$ and/or Zn
111 limitation, and possible, but unconfirmed, perturbations to the dissolved iron (dFe) cycle in coastal
112 Antarctic waters impacted by high rates of glacial ice melt and a warming climate.
113
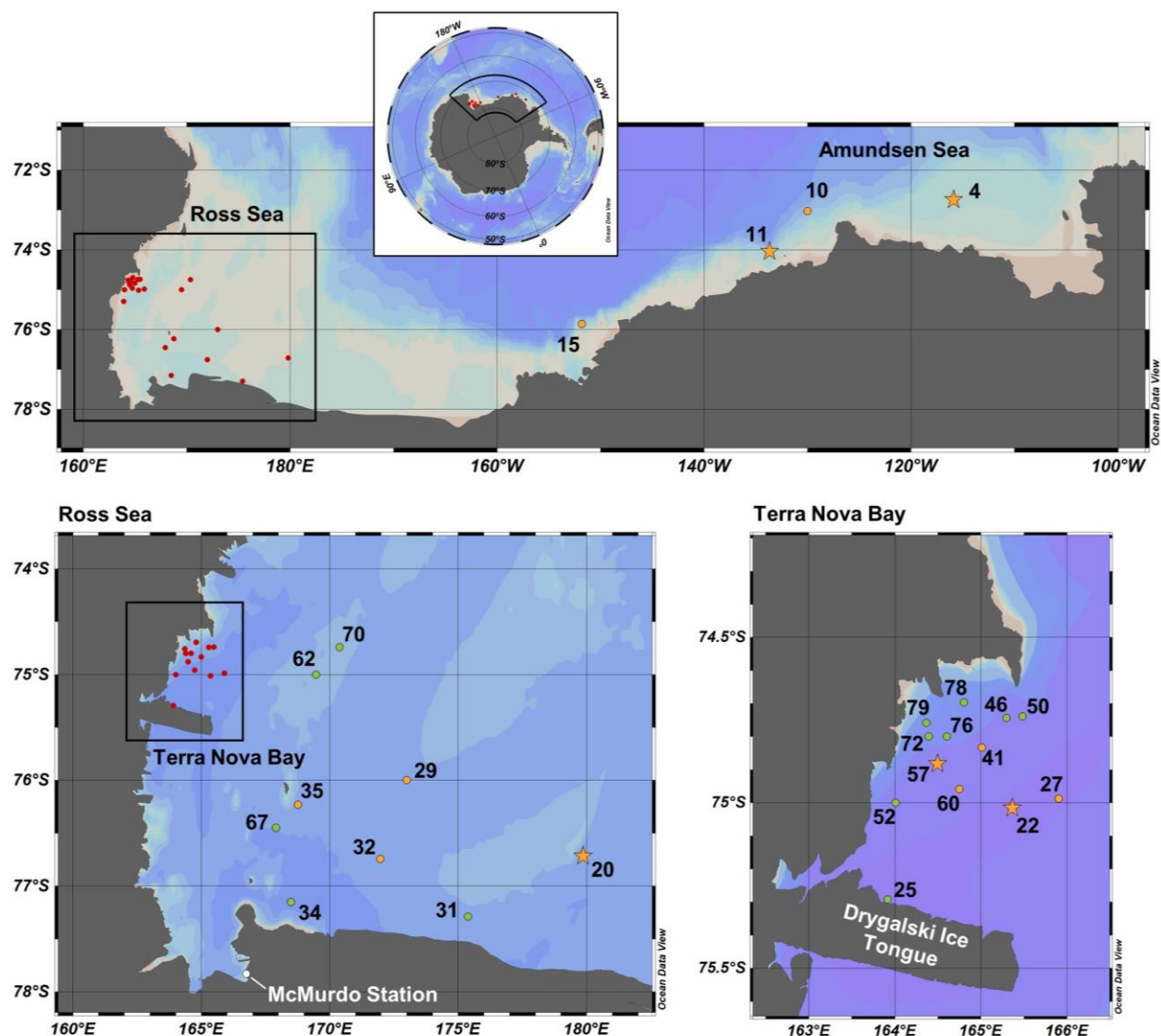
114
115 **Figure 1.** Map of CICLOPS stations in coastal Antarctic waters, including insets of stations within
116 the Ross Sea and Terra Nova Bay. Dissolved Co, dZn and dCd were analyzed at stations marked
117 in yellow, and stations marked in green were analyzed for dZn and dCd, but electrochemical dCo
118 measurements were not conducted. At stations marked with a star, Co, Zn and Cd uptake profiles
119 are presented in this study. Stations marked in red are shown in more detail in an inset. Note that
120 the grey coastline marks both terrestrial coastline and areas of consistent ice, including ice shelves
121 and glaciers; this includes the Drygalski Ice Tongue, a glacier to the south of Terra Nova Bay.

122

123 **2 Methods**

124 2.1 Study area and trace metal sampling

125   Samples were collected along the coastal Antarctic shelf from the Amundsen Sea, Ross
126 Sea, and Terra Nova Bay (Fig. 1) during the CICLOPS expedition on the RVIB *Nathanial B.*
127 *Palmer* (NBP-1801; December 16, 2017 – March 3, 2018). The expedition track first mapped a
128 transect from the Amundsen Sea, through the Ross Sea, and ending in Terra Nova Bay (Stations
129 4–22) over 10 days from December 31, 2017 to January 9, 2018, and then sampled at stations
130 between Terra Nova Bay and the western Ross Sea for the remainder of the expedition.

131   Dissolved seawater was collected from full-depth station profiles using a trace metal clean
132 sampling rosette deployed on a conducting synthetic line supplied by the U.S. Antarctic Program
133 (USAP) and equipped with twelve 8 L X-Niskin bottles (Ocean Test Equipment) supplied by the
134 Saito laboratory (Woods Hole Oceanographic Institution; Woods Hole, MA, USA). Real-time
135 trace metal rosette operations allowed for the careful collection of seawater from 10 and 20 m
136 above the ocean floor to study sediment-water interactions within a potential nepheloid layer. After
137 deployment, the X-Niskin bottles were transported to a trace metal clean-air van and pressurized
138 with high-purity (99.999 %) N_2 gas. Seawater samples for macronutrients, dCo and trace metal
139 analysis were then filtered through acid-washed 0.2 μM Supor polyethersulfone membrane filters
140 (Pall Corporation, 142 mm diameter) within 3 hours of rosette recovery.

141   To minimize metal contamination of samples, all sample bottles were prepared using trace
142 metal clean procedures prior to the expedition. The cleaning procedure for dCo sample bottles
143 entailed soaking sample bottles for ~1 week in Citranox, an acidic detergent, rinsing with Milli-Q
144 water (Millipore), soaking sample bottles for ~2 weeks in 10% trace metal grade HCl (Optima,
145 Fisher Scientific), and rinsing with lightly acidic Milli-Q water (< 0.1% HCl). Macronutrient
146 sample bottles were rinsed with Milli-Q water and soaked overnight in 10% HCl. The procedure
147 for total dissolved metal sample bottles (dZn and dCd) was identical to that used for dCo bottles
148 except the Citranox soak step was omitted.

149   Samples for dCo analysis were collected in 60 mL low-density polyethylene (LDPE)
150 bottles and stored at 4°C until analysis. Duplicate dCo samples were collected: one for at-sea
151 analysis of labile dCo and total dCo, and another for preservation and total dCo analysis in the
152 laboratory after the expedition. Preserved total dCo samples were stored with oxygen-absorbing
153 satchels (Mitsubishi Gas Chemical, model RP-3K), which preserve the sample for long-term
154 storage and future analysis (Noble et al., 2017; Bundy et al., 2020). Preserved dCo samples were
155 stored in groups of 6 within an open (unsealed) plastic bag, which was then placed into a gas-
156 impermeable plastic bag (Ampac) with one oxygen-absorbing satchel per 60 mL dCo sample. The
157 outer bag was then heat-sealed and stored at 4°C until analysis. Total dCo concentrations for
158 stations 57 and 60 were analyzed in the laboratory, while all other total dCo and labile dCo
159 concentrations were analyzed at sea.

160   Samples for total dissolved metal analysis (dZn and dCd) were collected in 250 mL LDPE
161 bottles and stored double-bagged at room temperature. After ~7 months, the total dissolved metals
162 samples were acidified to a pH of 1.7 with trace metal grade HCl (Optima, Fisher Scientific), and
163 were stored acidified for more than one year before instrumental analysis.

164 2.2 Dissolved Co and labile dCo analysis

165   Total dCo – the combined fractions of labile and ligand-bound dCo, hereafter simply dCo
166 – and labile dCo concentrations were analyzed via cathodic stripping voltammetry (CSV) as
167 described by Saito and Moffett (2001) and modified by Saito et al. (2010) and Hawco et al. (2016).
168 CSV analysis was conducted using a Metrohm 663 VA and µAutolabIII systems equipped with a
169 hanging mercury drop working electrode. All reagents were prepared as described in Chmiel et al.
170 (2022). Most samples were analyzed at sea within 3 weeks of sample collection, and stations 57
171 and 60 were analyzed for labile dCo at sea and their duplicate preserved samples were analyzed
172 for total dCo in November 2019 in the laboratory.

173   To measure total dCo concentrations, filtered seawater samples were first UV-irradiated in
174 quartz tubes for one hour in a Metrohm 705 UV Digester to destroy natural ligand-bound Co
175 complexes. 11 mL of sample was then added to a 15 mL trace metal clean polypropylene vial, and
176 100 µL of 0.1 M dimethyglyoxime (DMG; Sigma Aldrich) ligand and 130 µL of 0.5 M N-(2-
177 hydroxyethyl)piperazine-N-(3-propanesulfonic acid) (EPPS, Sigma Aldrich) buffer was added to
178 each sample vial. A Metrohm 858 Sample Processor then loaded 8.5 mL of each sample into the
179 electrode's Teflon cup and added 1.5 mL of 1.5 M $NaNO_2$ reagent (Merck). The mercury electrode
180 performed a fast linear sweep from -1.4 V to -0.6 V at a rate of 5 V s^{-1} and produced a cobalt
181 reduction peak at -1.15 V, the voltage at which the $Co(DMG)_2$ complex is reduced from Co(II) to
182 Co(0) (Saito and Moffett, 2001). The height of the Co reduction peak is linearly proportional to
183 the amount of total dCo present in the sample. Peak heights were determined by NOVA 1.10
184 software. A standard curve was created with 4 additions of 25 pM dCo to each sample, and a type-
185 I linear regression of the standard addition curve performed by the LINEST function in Microsoft
186 Excel allowed for the calculation of the initial amount of Co present in the sample.

187   When analyzing labile dCo concentrations, samples were not UV-irradiated so as to only
188 quantify the free or weakly bound dCo not bound to strong organic ligands. 11 mL of labile
189 samples were instead allowed to equilibrate with the DMG ligand and EPPS reagent overnight (~8
190 hours) before analysis to allow time for the labile dCo present in the sample to bind to the DMG
191 ligand via competitive ligand exchange (K > $10^{16.8}$). Labile dCo samples were then loaded onto
192 the Sample Processor and analyzed electrochemically using identical methods as described above
193 for total dCo samples.

194 2.3 Dissolved Co standards and blanks

195   During the CICLOPS expedition, an internal standard consisting of filtered, UV-irradiated
196 seawater was analyzed for dCo every few days while samples were being analyzed (39 ± 4 pM, n
197 = 9). While additional preserved dCo samples were analyzed in the laboratory in November 2019,
198 triplicate GSC2 GEOTRACES community intercalibration standards were carefully neutralized to
199 a pH of ~8 using negligible volumes of ammonium hydroxide (NH_4OH) and analyzed for dCo.
200 This is the same intercalibration batch originally reported in Table 1 of Chmiel et al. (2022), as
201 analysis for both expeditions overlapped temporally. The GSC2 standard was determined to have
202 a dCo concentration of 80.2 ± 6.2 (n = 3), a value that is very similar to the one reported by Hawco
203 et al., (2016) (77.7 ± 2.4). Currently, no official community consensus for dCo in the GSC2
204 intercalibration standard exists.

205   Analytical blank measurements for each reagent batch (a unique combination of DMG,
206 EPPS, and $NaNO_2$ reagent batches) were measured to determine any Co contamination due to
207 reagent impurities. Blanks were prepared in triplicate with UV-irradiated surface seawater passed
208 through a column with Chelex 100 resin beads (Bio-Rad) to remove metal contaminants, then UV-

209 irradiated again. Chelex beads were prepared as described in Price et al. (2013) to remove organic
210 impurities from leaching into the eluent. For the 5 batches of reagents used on this expedition, the
211 analytical blanks were found to be 2.3 pM, 4.0 pM, 10.1 pM, 15.6 pM, and 8.6 pM dCo, with an
212 average of 8.1 pM Co. The analytical blank detected for the laboratory-run total dCo samples was
213 1.0 pM. It should be noted that blank values above 10 pM are considered high for this method.
214 Analytical blank values were subtracted from the measured Co values determined with the
215 respective reagent batch. The average standard deviation within each triplicate batch of blanks (1.3
216 pM) was used to estimate the analytical limit of detection ($3 \times$ blank standard deviation) of 4 pM.
217 When detectable dCo concentrations were found below the 4 pM detection limit, their values were
218 preserved in the dataset and flagged as below the detection limit (<DL). In cases where no dCo or
219 labile dCo were detected (i.e., when no peak was measurable and/or the dCo value predicted was
220 < 0 pM), values of 0 pM were assigned for the purposes of plotting and selecting statistical analysis
221 and were flagged as not detected (n.d.) as well as <DL in the dataset; although these concentrations
222 were not detectable with our methodology, we believe the incredibly low concentrations of dCo
223 and labile dCo observed on this expedition were meaningful, and that removing these values from
224 our analysis misrepresents the data and would skew the results to appear higher than was observed.

225 **Table 1.** Mean dCo and labile dCo values measured in the surface ocean (10 m) and the deep
226 ocean (> 100 m) in the three regions sampled. One dCo sample and numerous labile dCo samples
227 were determined to be below the analytical detection limit (<DL) of 4 pM. Only using the values
228 measured above the detection limit would artificially inflate the calculation of the mean value;
229 instead, samples measured between 0 and the DL were left unaltered as their originally measured
230 value and samples with no detected concentrations of dCo or labile dCo (n.d.) were adjusted to 0
231 pM. The number of samples included in the mean calculation that are <DL is indicated by $n_{<DL}$.
232

		Surface (10 m)			
Region	**n**	dCo_{mean} **[pM]**	**dCo** $n_{<DL}$	**Labile** dCo_{mean} **[pM]**	**Labile dCo** $n_{<DL}$
Amundsen Sea	4	28 ± 7	0	5 ± 6	2
Ross Sea	4	28 ± 12	0	1 ± 2[a]	4
Terra Nova Bay	5	11 ± 7	1	UD[b]	5
		Deep (> 100 m)			
Region	**n**	dCo_{mean} **[pM]**	**dCo** $n_{<DL}$	**Labile** dCo_{mean} **[pM]**	**Labile dCo** $n_{<DL}$
Amundsen Sea	30	41 ± 5	0	4 ± 4	14
Ross Sea	32	46 ± 8	0	9 ± 7	9
Terra Nova Bay	34	39 ± 18	0	6 ± 8	18

233
234 [a] Of the 4 surface samples analyzed for labile dCo in the Ross Sea, 3 were n.d. and the fourth
235 contained 3.5 pM labile dCo.
236 [b] All surface samples in Terra Nova Bay were n.d. for labile dCo.

237 2.4 Dissolved Zn and Cd analyzed by ICP-MS

238   Total dissolved trace metal samples were analyzed for dZn and dCd using isotope dilution
239 and inductively coupled plasma mass spectrometry (ICP-MS) as described in Kellogg et al.
240 (Submitted) based on methodology described in Cohen et al. (2021). Briefly, 15 mL of acidified

241 filtered seawater samples were spiked with an acidified mixture of stable isotopes including ^{67}Zn,
242 and ^{110}Cd, among other metal stable isotopes, and pre-concentrated via a solid phase extraction
243 system seaFAST-pico (Elemental Scientific) to an elution volume of 500 µL. The samples were
244 then analyzed using an iCAP-Q ICP-MS (Thermo Scientific) and concentrations were determined
245 using a multi-elemental standard curve (SPEX CertiPrep).

246 2.5 Co, Zn and Cd uptake rates via isotope incubations

247 Co, Zn and Cd uptake rates were quantified using incubations of collected marine microbial
248 communities spiked with stable or radioisotopes to trace the conversion of dissolved trace metal
249 into the particulate phase. Briefly, unfiltered seawater used for the incubation uptake experiments
250 was collected from the trace metal rosette, and the Co, Zn and Cd uptake incubations were spiked
251 with 0.1 pM ^{57}CoCl$_2$, 2 nM ^{67}ZnO and 300 pM ^{110}CdO, respectively. All incubation bottles were
252 then sealed and placed in a flow-through shipboard incubator on the deck that exposed the
253 incubations to a natural day/night cycle and surface-temperature seawater for 24 hours. The
254 incubator was shielded by black mesh screening to allow 20% ambient light penetration.
255 Incubation biomass was collected by vacuum filtration onto acid-rinsed 3 µm Versapor filters
256 (Pall). The ^{57}Co incubation filters were stored at room temperature in Petri dishes prior to
257 radiochemical gamma-ray counting both at sea and in the laboratory, and the ^{67}Zn and ^{110}Cd
258 incubation filters were stored at -80 ºC in acid-rinsed cryovials until ICP-MS analysis in the
259 laboratory. See Kellogg et al. (Submitted), Rao 2020 and Kellogg (2022) for full methodology and
260 instrumental analysis.

261 2.6 Pigment and phosphate analysis

262 Phytoplankton pigment samples were collected from a non-trace metal rosette deployed
263 separately from the trace metal rosette, and were filtered and analyzed for select pigments by high-
264 performance liquid chromatography (HPLC) as described in DiTullio and Geesey (2003).
265 Macronutrient samples were collected from the trace metal rosette alongside dCo samples and
266 were filtered using the same methodology as dCo and total metal samples (see above). Samples
267 were collected in 60 mL high-density polyethylene (HDPE) bottles and were stored frozen until
268 analysis. Dissolved PO$_4$ concentrations were determined by Joe Jennings at Oregon State
269 University via the molybdenum blue method (Bernhardt and Wilhelms, 1967) using a Technicon
270 AutoAnalyzer II attached to an Alpkem autosampler.

271 2.7 Historical dCo and pigment data

272 In this study, dCo profiles from the CICLOPS expedition are compared to those from
273 previous fieldwork in the Ross Sea, including the Controls of Ross Sea Algal Community Structure
274 (CORSACS) expeditions: CORSACS-1 (NBP-0601; December 27, 2005 – January 23, 2006) and
275 CORSACS-2 (NBP-0608; November 8, 2006 – December 3, 2006), reported in Saito et al. (2010),
276 and fieldwork sampling the water column under the sea ice of the McMurdo Sound (November 9
277 – 23, 2009), reported in Noble et al. (2013). The locations of stations used in this study from the
278 CORSACS-1 expedition, CORSACS-2 expedition, and McMurdo Sound fieldwork are given with
279 respect to CICLOPS stations in Fig. A1. Dissolved cobalt and pigment data from these three
280 fieldwork expeditions were sampled and analyzed with comparable methodologies as those used
281 on the CICLOPS expedition, and the CORSACS data are accessible online at https://www.bco-
282 dmo.org/dataset/3367.

283 2.8 Statistical Analysis

284   The linear regressions presented in this study are two-way (type-II) linear regressions, with
285 the exception of the standard addition curves used to calculate dCo concentrations (Sect. 2.2).
286 Two-way regressions are ideal for stoichiometric ratios because they allow for error in both the x
287 and y parameters and do not assume dependence between the x and y axes. The two-way regression
288 function used in this study was rewritten to Python from a MATLAB file (lsqfitma.m) originally
289 written by Ed Pelzer circa 1995 (Chmiel et al., 2022) and is available at https://github.com/rebecca-
290 chmiel/GP15.

291   Independent t-tests were performed using the stats.ttest_ind function within statistical
292 function module of the SciPy Python library.

293 **3 Results**

294 3.1 Dissolved Co distribution and speciation

295   During the CICLOPS expedition, full-depth profiles of dCo and labile dCo samples were
296 analyzed from 13 stations in the Amundsen Sea (Stations 4, 10, 11, 15), the Ross Sea (Stations 20,
297 29, 32, 35) and Terra Nova Bay (Stations 22, 27, 41, 57, 60; Fig. 1). The resulting dCo profiles
298 (Fig. 2) show depletion in the surface ocean consistent with a nutrient-type profile; at 10 m depth,
299 dCo concentrations were found to be 28 ± 7 pM in the Amundsen Sea (n = 4), 28 ± 12 pM in the
300 Ross Sea (n = 4), and only 11 ± 7 pM in Terra Nova Bay (n = 5; Table 1). Labile dCo distributions
301 generally followed those of dCo, and also showed strong depletion in the surface ocean. In the
302 Amundsen and Ross Seas, surface (~10 m) labile dCo concentrations ranged between 12 pM at
303 station 10 and undetected (n.d.) concentrations at stations 15, 20, 32 and 35. In Terra Nova Bay,
304 no surface labile dCo concentrations were detected at any of the 5 stations sampled, indicating that
305 the dCo inventory was dominated by the strongly ligand-bound dCo fraction.

306   In the deep ocean (≥ 100 m depth), dCo distributions were relatively consistent throughout
307 the water column, with the exception of elevated concentrations of dCo at near-bottom depths. The
308 Amundsen Sea, Ross Sea, and Terra Nova Bay all displayed similar deep dCo concentrations of
309 41 ± 5 pM (n = 30), 46 ± 8 pM (n = 32), and 39 ± 18 pM (n = 34), respectively (Table 1). The high
310 standard deviation of deep dCo in Terra Nova Bay is partially driven by the elevated near-seafloor
311 signal at Station 41 (770 m and 780 m); when the two deepest points at Station 41 are omitted, the
312 average deep dCo in Terra Nova Bay was 36 ± 10 pM. The CICLOPS expedition included regular
313 near-bottom sampling as allowed by the altimeter aboard the trace metal rosette. As a result, many
314 of the deepest profile samples contained elevated concentrations of dCo and labile dCo along the
315 seafloor, including stations 20, 22, 27, 29, 32, 41 and 57. This deep dCo signal was particularly
316 observable in stations where two near-seafloor samples were taken: one ~10 m above the seafloor
317 and a second ~20 m above the seafloor. At stations 41 and 57, the elevated near-seafloor dCo
318 signal was pronounced (Fig. 2); the samples ~10 m above the seafloor contained 111 pM and 50
319 pM dCo, respectively, which represents a 31 pM and 18 pM increase, respectively, from the
320 samples collected ~20 m above the seafloor. This finding indicates that dCo was elevated in a
321 narrow band close to the seafloor, and it is likely that dCo concentrations continued to increase in
322 the 10 m between the deepest samples and the seafloor.
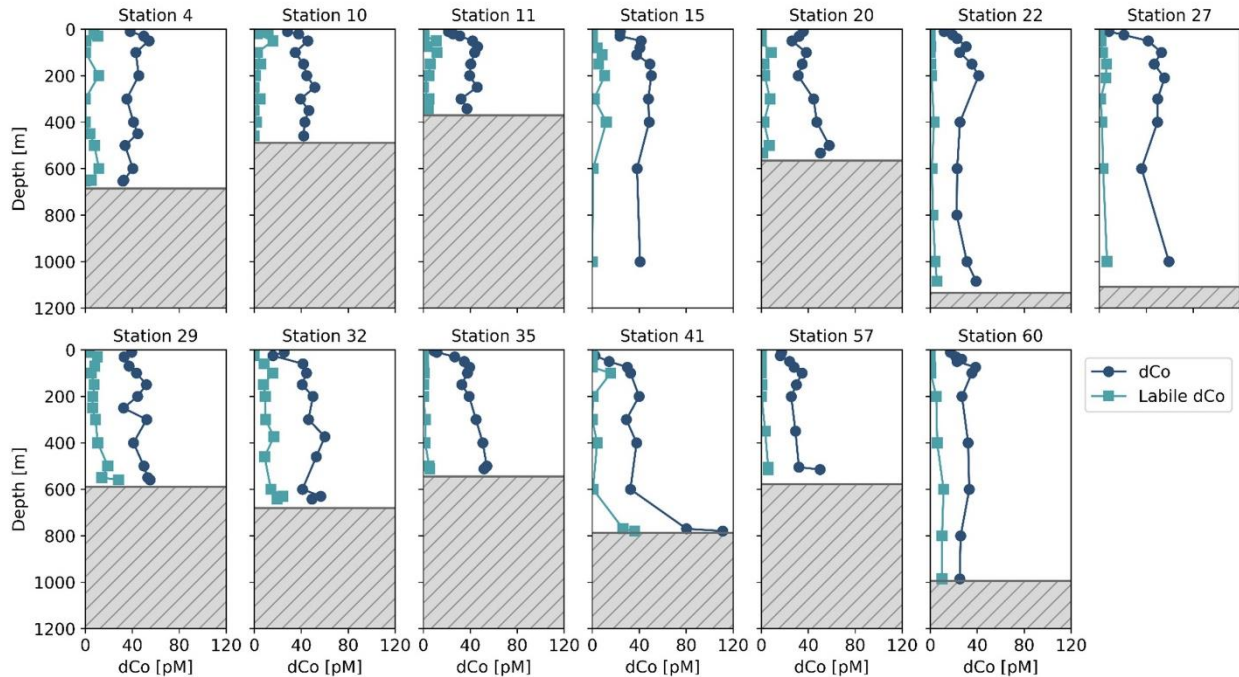
Figure 2. Dissolved Co and labile dCo full-depth profiles from the CICLOPS expedition to the Amundsen Sea (Stations 4, 10, 11, 15), Ross Sea (Stations 20, 29, 32, 35) and Terra Nova Bay (Stations 22, 27, 41, 57, 60). The top of the grey box marks the location of the seafloor.

3.2 Phytoplankton communities in the Amundsen Sea, Ross Sea and Terra Nova Bay

Stations 11, 15, 22 and 27 exhibited high surface chlorophyll-a (Chl-a) fluorescence (17–42 mg m^{-3} at 10 m), characteristic of phytoplankton blooms. The Amundsen Sea stations displayed high concentrations of 19'-hexanolyoxyfucoxanthin (19'-Hex), a pigment commonly used as a proxy for haptophyte biomass. In the coastal Southern Ocean, 19'-Hex is often correlated with *Phaeocystis antarctica* (DiTullio and Smith, 1996; DiTullio et al., 2003), and it is typical to find concentrated blooms of *P. antarctica* in these regions, particularly during the highly productive spring blooms of the Antarctic polynyas (Arrigo et al., 1999; DiTullio et al., 2000). The pigment fucoxanthin (Fuco) is commonly used as a proxy for diatom biomass, although it can also be produced by haptophytes like *P. antarctica* growing under Fe-replete conditions (DiTullio et al., 2003; DiTullio et al., 2007); Fuco was observed at stations throughout the expedition and tended to be relatively consistent throughout the CICLOPS stations, particularly in comparison to 19'-Hex, which displayed very high concentrations at some stations and much lower concentrations at others. In general, higher concentrations of Fuco were observed within Terra Nova Bay as well as at stations sampled later in the summer season. This is consistent with past observations of summer diatom blooms, which tend to occur after the annual spring bloom where and when dFe is available (Sedwick et al., 2000; Peloquin and Smith, 2007; Saito et al., 2010).

The upper ocean inventories of three pigments, 19'-Hex, Fuco and Chl-a, a proxy for general phytoplankton biomass in the Southern Ocean, were estimated via trapezoidal integration of their profiles between 5 and 50 m depth and compared to the 2005/2006 summer bloom observed on the CORSACS-1 expedition (Fig. 3). In the Ross Sea and Terra Nova Bay, CICLOPS stations contained smaller inventories of Chl-a and 19'-Hex compared to the Amundsen Sea, likely reflecting the end of the spring bloom and transition to a summer phytoplankton assemblage in

350 these regions. One noticeable difference between the overlapping 2006 and 2018 January seasons
351 is the larger Fuco inventory in 2006 in both the Ross Sea and Terra Nova Bay compared to the
352 2018 season, indicating a larger presence of diatom biomass during the CORSACS-1 expedition
353 compared to the CICLOPS expedition despite relatively similar Chl-a inventories.
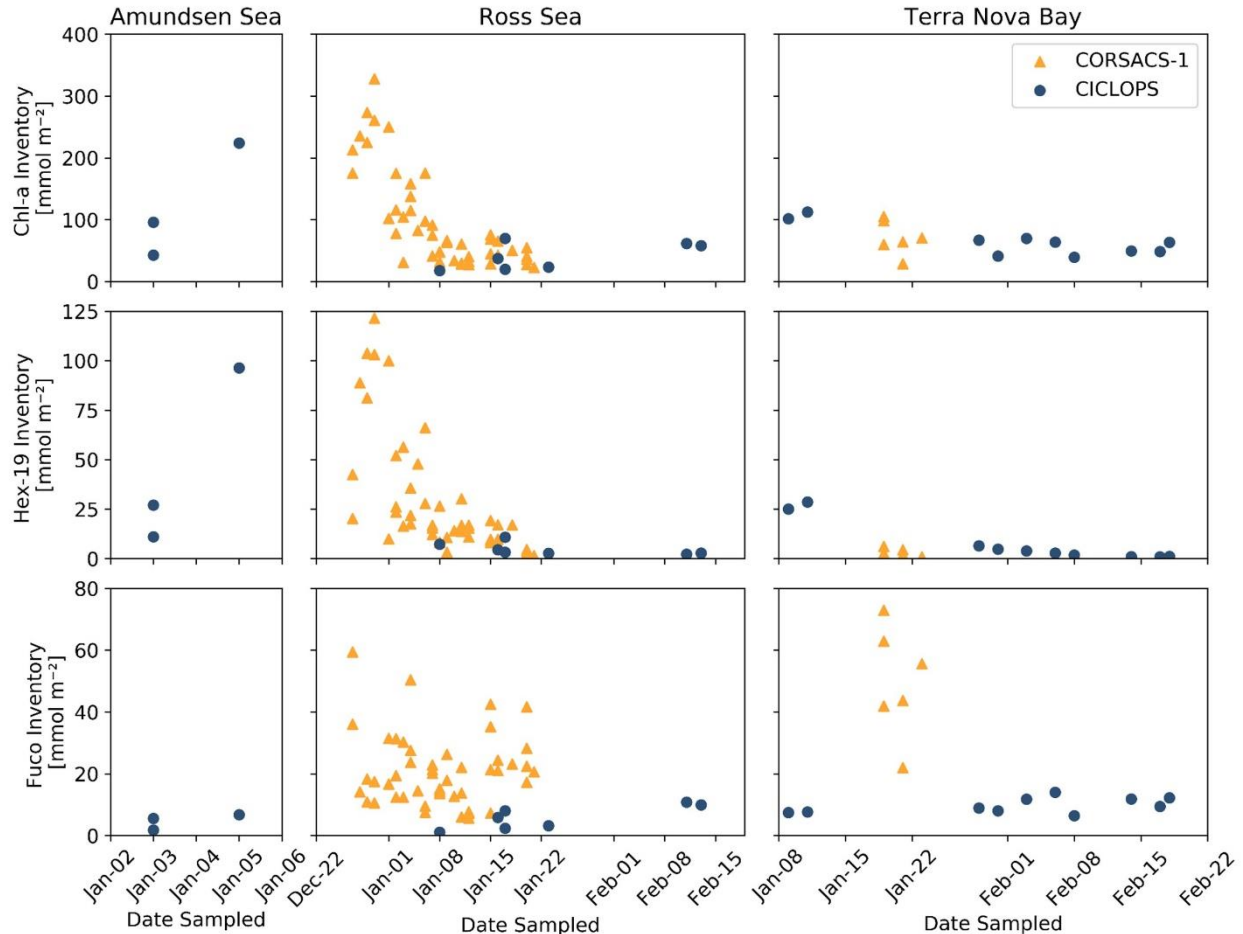
354
355 **Figure 3.** Upper ocean inventories of Chlorophyll-a (Chl-a), 19'-hexanolyoxyfucoxanthin (19'-
356 Hex) and fucoxanthin (Fuco) plotted over the austral summer season for both the 2005/2006
357 CORSACS-1 and 2017/2018 CICLOPS expeditions. Inventories were estimated via trapezoidal
358 integration of the pigment depth profiles between 5 and 50 m depth. Note that the dates along the
359 x-axis are not continuous between plots of each region, and the y-axis scales differ among the 3
360 pigments.

361 3.3 dZn, dCd and trace metal uptake rates

362   Dissolved Cd and Zn profiles, as well as trace metal uptake rate (ρM) profiles for Co, Zn
363 and Cd from the CICLOPS expedition were originally presented in Rao (2020) and Kellogg
364 (2022). This study presents a comparison between dCo distribution and the distribution and uptake
365 of dZn and dCd, two trace metals linked with Co biogeochemical cycling since all three metals are
366 known to share similar uptake transporter pathways and can be interchangeably utilized as
367 cofactors within specific classes of the enzyme carbonic anhydrase (Sunda and Huntsman, 1995,
368 2000; Saito and Goepfert, 2008; Kellogg et al., 2020, 2022).

The dZn and dCd profiles observed on the CICLOPS expedition displayed nutrient-like structure, with depleted concentrations near the surface (Fig. 4). In the deep ocean ($\geq$100 m), dZn and dCd concentrations were relatively uniform, displaying average deep concentrations of 4.6 ± 1.1 nM (n = 182) and 700 ± 90 pM, respectively (Table 2). Average dissolved metal concentrations in the surface ocean (10 m depth) were higher in the Amundsen Sea (2.5 ± 1.2 nM dZn; 450 ± 170 pM Cd) compared to the Ross Sea (1.1 ± 1.2 nM dZn; 250 ± 170 pM dCd) and Terra Nova Bay (0.87 ± 0.42 nM dZn; 130 ± 170 pM dCd). This trend of decreasing surface dissolved metals from the Amundsen to Terra Nova Bay was mirrored in the dCo distributions, and could be explained by the seasonal drawdown of metal nutrients in the mixed layer over time, differences in the metal uptake of phytoplankton in the different regions, or both phenomenon occurring simultaneously.

At Stations 4, 11, 20, 22 and 57, uptake rates of Co, Zn and Cd within seawater collected from 0–200 m were determined via spiked-isotope incubations (Rao, 2020; Kellogg, 2022). The relative ratios of the resulting uptake profiles from biomass collected onto 3 μm filters provide insight into the demand for Co, Zn and Cd of eukaryotic phytoplankton in coastal Antarctica (Fig. 5). Note that Co uptake within the bacterial size fraction (0.2–3 μm) was also analyzed and the results are presented in Rao (2020), but here we present the results of the eukaryotic size fraction (> 3 μm) to best represent the eukaryotic phytoplankton community present and compare to the Zn and Cd uptake experiments. It should be noted that uptake rates measured via tracer addition and shipboard incubations represent potential uptake and may be overestimations of the environmental nutrient uptake rates because the isotope tracer addition was labile – not at equilibrium with the natural seawater ligands – and could have perturbated the natural micronutrient inventories. The $^{57}CoCl_2$ addition (0.1 pM) was likely a small enough addition that the inventory was not significantly disturbed, but added concentrations of ^{67}ZnO (2 nM) and ^{110}CdO (300 pM) were not tracer-level additions and necessarily increased the existing trace metal inventories, possibly leading to the overestimation of total metal uptake rates (Rao, 2020; Kellogg, 2022).

Table 2. Mean dZn and dCd values from the surface ocean (10 m) and the deep ocean (> 100 m) in the three regions sampled.

Region	Surface (10 m)			
	dZn_{mean} [nM]	n_{dZn}	dCd_{mean} [pM]	n_{dCd}
Amundsen Sea	2.6 ± 1.2	4	450 ± 170	4
Ross Sea	1.1 ± 1.2	6	250 ± 170	7
Terra Nova Bay	0.87 ± 0.42	11	130 ± 60	11
All	1.3 ± 1.0	21	230 ± 170	22
Region	Deep (> 100 m)			
	dZn_{mean} [nM]	n_{dZn}	dCd_{mean} [pM]	n_{dCd}
Amundsen Sea	5.4 ± 0.6	30	730 ± 40	30
Ross Sea	4.7 ± 0.6	65	740 ± 80	65
Terra Nova Bay	4.3 ± 1.4	87	670 ± 100	90
All	4.6 ± 1.1	182	700 ± 90	185
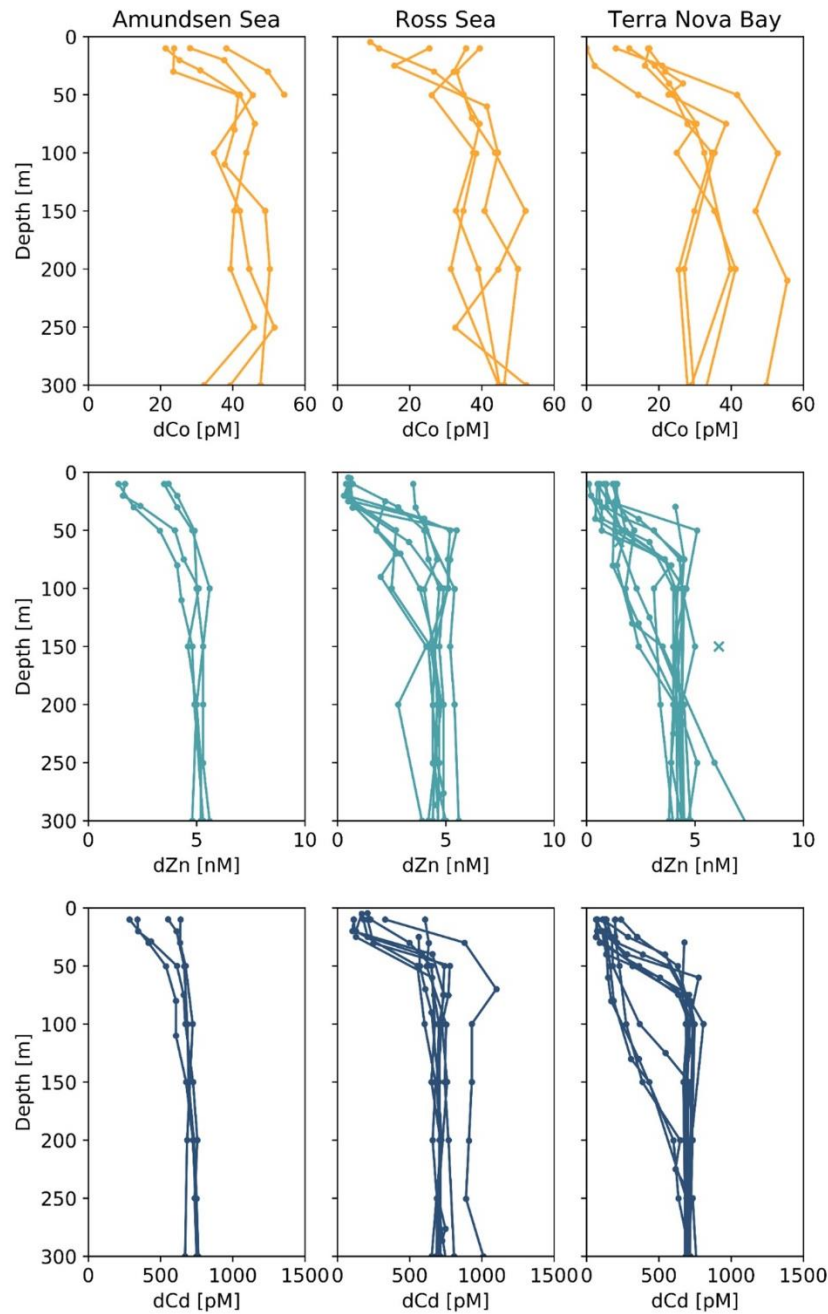
398
399 **Figure 4.** Upper ocean trace metal depth profiles of dCo, dZn and dCd, by region (left panels,
400 Amundsen Sea; middle panels, Ross Sea; right panels, Terra Nova Bay). Outliers are marked with
401 an 'x'. Dissolved Zn and Cd profile data are further described in Kellogg (2022).
402
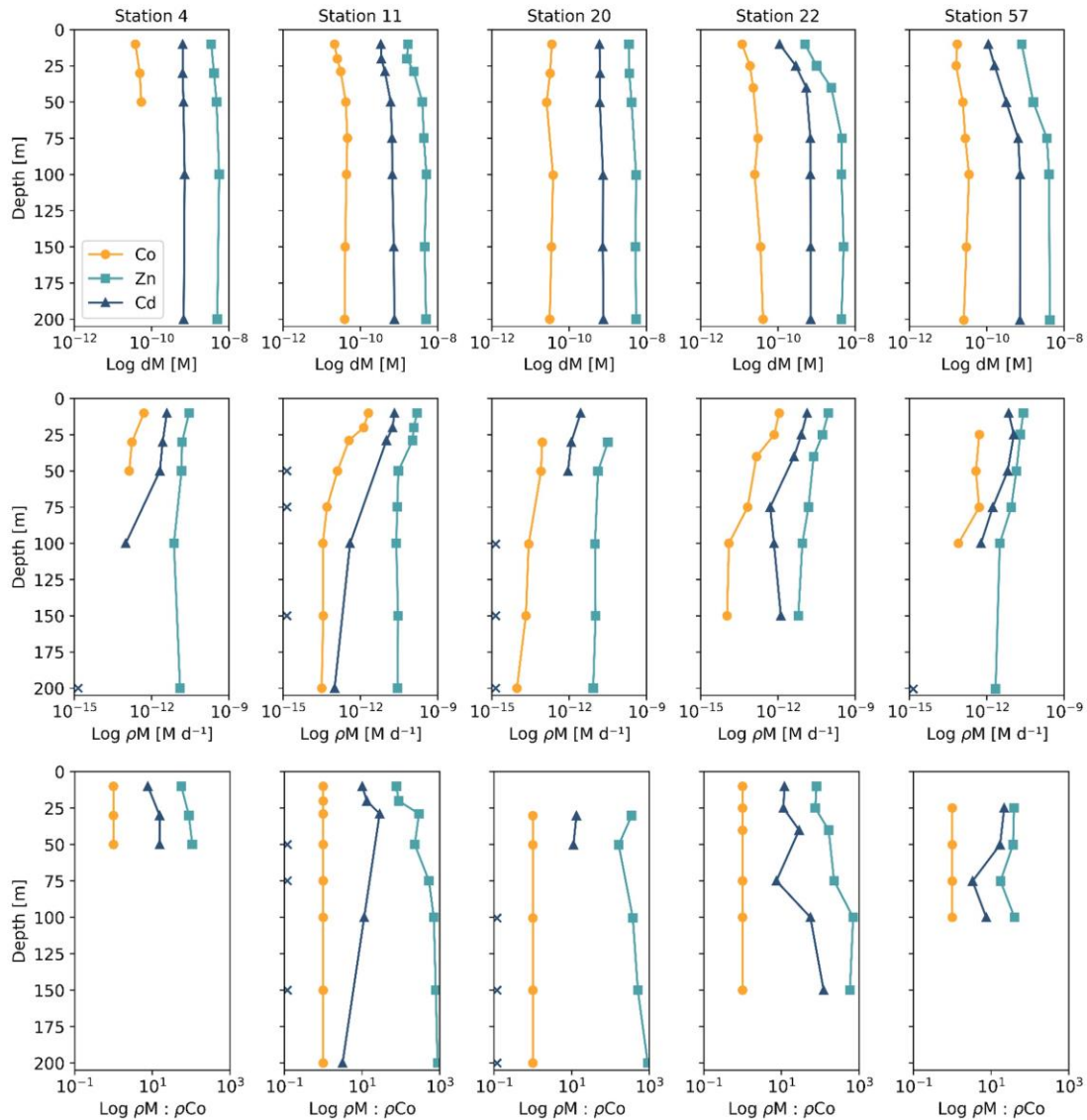
Figure 5. Depth profiles of dissolved metals (dM; top), trace metal uptake rates (ρM; middle), and trace metal uptake rates normalized to the uptake rate of dCo (ρM : ρCo), plotted along a log scale. Stations 4 and 11 are from the Amundsen Sea, Station 20 is from the Ross Sea, and Stations 22 and 57 are from Terra Nova Bay. Depths at which an uptake rate is below detection (specifically for ρCd) are marked with an 'x' along the y-axis. Co trace metal uptake data are further described in Rao (2020) and Zn and Cd uptake data are further described in Kellogg (2022).

Of the five stations with uptake rate data from all three trace metals of interest, four (Stations 4, 11, 20 and 22) were from a transect conducted from the Amundsen Sea to Terra Nova Bay, and were sampled within a span of 10 days from December 31, 2017 to January 9, 2018, while the last station (Station 57) was sampled later in the summer on February 6, 2018; this range of stations allows us to assess the uptake stoichiometry along both spatial (location) and time (bloom progression) dimensions. The ρM profiles displayed an increase in metal uptake of Co, Zn and Cd towards the surface, a shape which was mirrored in the lower dissolved trace metal concentrations of the surface ocean, suggesting the influence of phytoplankton uptake on the

418 drawdown of micronutrients in the photic zone. The stoichiometry of ρM among Co, Zn and Cd
419 tended to directly follow the metals' availability as dissolved species: Co, which is present at the
420 lowest concentrations of ~10^{-11} M, was taken up at rates ranging between 10^{-13} and 10^{-12} M d^{-1};
421 Cd, at concentrations of ~10^{-10} M, was taken up at rates of 10^{-12} to 10^{-11} M d^{-1}; and Zn, present in
422 the highest concentration of ~10^{-9} M, was taken up at rates of 10^{-12} to 10^{-10} M d^{-1}. This observation
423 reveals order-of-magnitude differences in biological uptake between the three metals, matching
424 patterns of metal availability in the water column.

4 Discussion

425

426 4.1 Biogeochemical Co cycle processes observed via dCo profiles and dCo : dPO$_4^{3-}$ stoichiometry

427   Low surface ocean dCo and labile dCo concentrations are attributable to uptake by
428 phytoplankton and bacteria in the Southern Ocean, giving the dCo and labile dCo vertical profiles
429 a distinct nutrient-like shape (Fig. 2). The labile dCo fraction was extremely low or below the limit
430 of detection in surface waters, particularly within Terra Nova Bay, indicating strong drawdown of
431 the labile fraction and near 100% complexation of dCo in the water column. Labile dCo is
432 considered to be more bioavailable than strongly-bound dCo and thus is likely preferentially taken
433 up by microbes when available. This labile dCo may then be rapidly cycled by phytoplankton in
434 the mixed layer and any labile dCo released via remineralization, cell lysis, or grazing would be
435 promptly taken up by other algae and microbes. A rapid turnover of labile dCo suggests a high
436 demand for bioavailable Co from the surface phytoplankton community.

437   Dissolved Co and PO$_4$ displayed a generally positive relationship in the upper ocean, which
438 is indicative of the co-cycling of both nutrients via phytoplankton uptake and remineralization
439 (Fig. 6a). The processes of biological uptake and remineralization, when observed along dCo vs.
440 dPO$_4^{3-}$ axes, can be represented by vectors with positive slopes and opposite directionality. Abiotic
441 dCo inputs and Co scavenging processes can be represented by vertical or near-vertical vectors
442 because they decouple the cycling of dCo and dPO$_4^{3-}$. The positive dCo vs. dPO$_4^{3-}$ linear
443 relationship that is often observed within the ocean's mixed layer can exhibit a variety of slopes
444 that are dictated by the nutrient uptake and remineralization stoichiometry of the microbial
445 community (Saito et al., 2017). On CICLOPS, the dCo vs. dPO$_4^{3-}$ relationship displayed a
446 drawdown of both dCo and dPO$_4^{3-}$ in the upper ocean, and the labile dCo vs. dPO$_4^{3-}$ relationship
447 revealed the stark lack of labile dCo throughout the upper ocean (Fig. 6b,d). The dCo vs. dPO$_4^{3-}$
448 slope in the upper ocean (0–100 m depth) was found to be distinct for each of the three regions
449 sampled on the expedition; the Ross Sea displayed the highest slope (74 ± 18 µmol : mol), followed
450 by the Amundsen Sea (47 ± 9 µmol : mol) and Terra Nova Bay, which displayed the lowest dCo
451 vs. dPO$_4^{3-}$ slope (26 ± 4 µmol : mol; Fig. 7; Table 3). These slopes reflect a relatively wide range
452 of dCo stoichiometries that vary by a factor of 2.8 between the lowest and highest slopes observed.
453 For comparison, the 2005/2006 CORSACS-1 and CORSACS-2 Ross Sea data points were pooled
454 and the dCo vs. dPO$_4$ slope was recalculated (originally reported as 37.6 µmol : mol between 5–
455 500 m depth; Saito et al., 2010) to fall within the same depth window (0–100 m). The resulting
456 slope fell within the range of slopes observed on CICLOPS (49 ± 4 µmol : mol; R^2 = 0.57; n =
457 106).

458   The range of dCo vs. dPO$_4^{3-}$ slopes reflects the elasticity of cobalt uptake stoichiometry in
459 the upper ocean, which varies by microbial community and the availability of dCo and other
460 nutrients. Due to the number of factors that can affect the environmental stoichiometry of trace

461 metal nutrients, the dCo vs. dPO$_4^{3-}$ slope must be interpreted alongside other information about
462 the marine environment, such as the available dCo inventory and the local nutrient limitation
463 regime, making global comparisons of dCo : dPO$_4^{3-}$ stoichiometry complex. The lower
464 stoichiometric slope observed in Terra Nova Bay compared to the Ross and Amundsen Seas likely
465 indicates not a lack of demand for Co by phytoplankton, but the low availability of Co in the
466 surface ocean despite high demand for the metal. Terra Nova Bay was found to have the lowest
467 average surface dCo, dZn and dCd concentrations of the three regions studied, and both Terra
468 Nova Bay stations where ρCo was measured (Stations 22 and 57) displayed higher surface Co
469 uptake rates (0.71 and 0.51 pM d^{-1}, respectively, at 25 m depth) than Station 20 in the Ross Sea
470 (0.09 pM d^{-1} at 30 m depth). It is likely that the lower dCo stoichiometry in Terra Nova Bay was
471 driven by nutrient draw-down and low availability of labile dCo in the region resulting from
472 productive phytoplankton blooms. Remineralization would also have played a role in setting the
473 dCo vs. dPO$_4$ slope below the photic zone; a remineralization vector with a relatively low slope
474 indicates that there was a lower dCo source from particulate Co biomass and a rapid turnover of
475 recycled dCo back into biomass, suggesting a tight coupling of the dissolved and particulate
476 phases.

477

478 **Table 3.** Trace metal : dPO$_4^{3-}$ stoichiometric regressions for dCo, dZn and dCd in both the surface
479 and deep ocean of the Amundsen Sea, Ross Sea and Terra Nova Bay, as shown in Fig. 7. Linear
480 regression slopes with $R^2 < 0.50$ are not shown as the slope values should not be considered
481 meaningful stoichiometric values.

482

Region	dCo:dPO$_4^{3-}$ [µmol:mol]				dZn:dPO$_4^{3-}$ [mmol:mol]				dCd:dPO$_4^{3-}$ [mmol:mol]			
	Depths [m]	n	Slope	R^2	Depths [m]	n	Slope	R^2	Depths [m]	n	Slope	R^2
Amundsen Sea												
Surface	0-100	16	47 ± 9	0.64	0-30	9	4.6 ± 0.9	0.72	0-25	6	0.47 ± 0.08	0.86
Deep	>100	20	--	0.02	>30	35	--	0.37	>25	38	0.59 ± 0.06	0.72
Ross Sea												
Surface	0-100	15	74 ± 18	0.53	0-30	11	--	0.07	0-25	11	0.19 ± 0.05	0.56
Deep	>100	24	--	0.21	>30	77	9.8 ± 1.0	0.54	>25	79	--	0.26
Terra Nova Bay												
Surf	0-100	20	26 ± 4	0.65	0-50	24	1.9 ± 0.3	0.65	0-30	21	0.15 ± 0.03	0.59
Deep	>100	26	--	0.05	>50	95	--	0.30	>30	104	0.64 ± 0.03	0.80

483

484 Deviations from the linear uptake-remineralization line in the dCo vs. dPO$_4^{3-}$ relationship
485 occur when dCo distributions become decoupled from dPO$_4^{3-}$ or vice versa, as with Co scavenging
486 onto particles and lithogenic dCo sources. In other ocean regions, the dCo vs. dPO$_4^{3-}$ relationship
487 displays a characteristic "curl" towards the high- dPO$_4^{3-}$, low-dCo in deeper waters, resulting from
488 the net vector sum of both remineralization, which increases both dPO$_4^{3-}$ and dCo, and scavenging
489 to Mn-oxides, which removes dCo in excess of dPO$_4^{3-}$ from the water column (Noble et al., 2008;
490 Hawco et al., 2017; Saito et al., 2017). The dCo vs. dPO$_4^{3-}$ relationship observed on CICLOPS,
491 however, displayed no such scavenging curl, indicating no clear signal of dCo loss due to
492 scavenging, at least within timescales relevant to water column mixing. This finding is consistent
493 with previous studies of the Ross Sea that have also observed little evidence of dCo loss via
494 scavenging in the mesopelagic (Saito et al., 2010; Noble et al., 2013). The lack of a visible
495 scavenging signal may be attributable to the deep winter mixed layers of coastal Antarctic seas
496 that reach depths of up to 600 m and can extend to the seafloor (Smith and Jones 2015). This deep

497 vertical mixing allows the dCo : dPO$_4^{3-}$ ratio in the deep ocean to reset on an annual timescale,
498 potentially erasing any signals of dCo scavenging, which would be expected to occur on a
499 timescale of decades to centuries (Hawco et al., 2017). Additionally, Oldham et al. (2021)
500 concluded that a suppressed Co scavenging flux might be the result of a unique Mn cycle in the
501 Ross Sea, characterized by low to undetectable concentrations of Mn-oxide particles, slow rates
502 of Mn-oxide formation, and the stabilization of organic dMn via Mn(III) ligands (Oldham et al.,
503 2021).
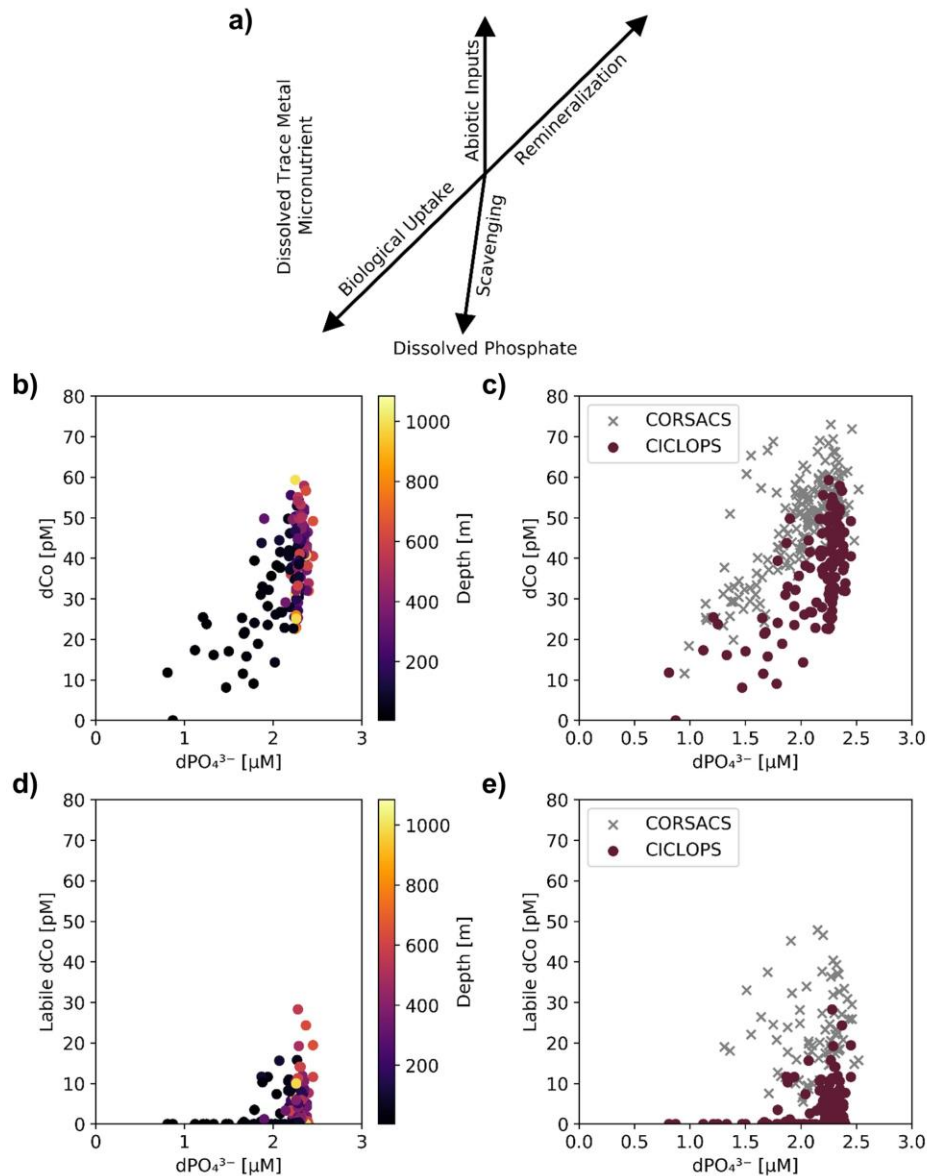
504
505 **Figure 6. (a)** A vector schematic of the relationship between dPO$_4^{3-}$ and dissolved trace metals
506 like dCo, and how the various marine processes can affect their distribution and environmental
507 stoichiometry. Adapted from Noble et al. (2008). The CICLOPS **(b)** dCo vs. dPO$_4^{3-}$ relationship
508 and **(d)** labile dCo vs. dPO$_4^{3-}$ relationship, plotted by depth. Also shown are the CICLOPS (red)
509 **(c)** dCo vs. dPO$_4^{3-}$ and **(e)** labile dCo vs. dPO$_4^{3-}$ samples overlaid with CORSACS (gray) samples.
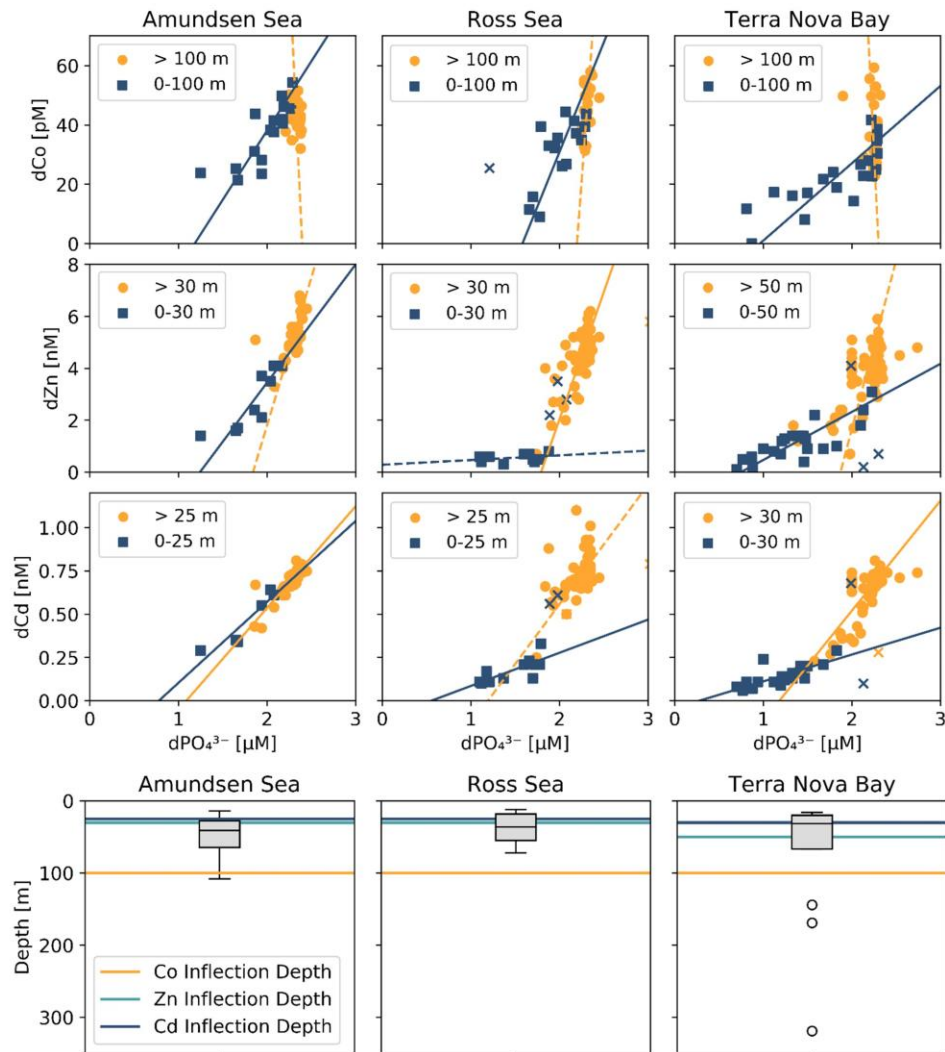
Figure 7. (Top 3 rows) Trace metal : dPO_4^{3-} relationships from the three CICLOPS regions sampled, divided into upper ocean (blue square) and deep ocean (orange circle) bins with a manual depth threshold (or inflection point depth) selected to optimize the linear fit of the upper and deep ocean trends. Regressions with an $R^2 \geq 0.50$ are shown as a solid line, and those with an $R^2 < 0.50$ are shown as a dotted line. The results of the linear regressions are given in Table 3. Regression outliers were selected by hand when including them in the linear regression substantially decreased its R^2 value; outliers are marked with an 'x'. (Bottom row) The inflection point depths assigned to dCo, dZn and dCd relationships are shown compared to a box and whiskers plot of the mixed layer depths, with mixed layer depth outliers marked with an 'o'.

4.2 Elevated dCo concentrations within a benthic nepheloid layer

The elevated dCo signal observed from several depths within 20 m of the seafloor were sourced from a benthic nepheloid layer: a near-seafloor region of the water column characterized by high particle abundance, turbulence, and isopycnal movement of both dissolved and particulate material along the seafloor (Gardner et al., 2018). The Ross Sea has been observed to display strong nepheloid layers as cold, dense water flows northward along the Ross Sea shelf until it

526 reaches the shelf break, carrying suspended sediments with it along the seafloor (Budillon et al.,
527 2006). Nepheloid layers tend to be enriched in dissolved trace metals like dFe, and can act as a
528 source of micronutrients if upwelled to the surface ocean (Marsay et al., 2014; Noble et al., 2017).
529 Elevated dCo concentrations within the Ross Sea nepheloid layer is a novel finding, as previous
530 expeditions analyzing dCo concentrations in the Ross Sea did not sample as close to the seafloor
531 as the CICLOPS trace metal rosette was able to (Fitzwater et al., 2000; Saito et al., 2010; Noble et
532 al., 2013). This finding is evidence of a dCo source to the deep ocean that may be upwelled to
533 intermediate and upper ocean waters via vertical mixing.

534 4.3 Decreased Ross Sea dCo and labile dCo inventories

535   The dCo and labile dCo profiles observed along the 2017/2018 CICLOPS expedition
536 displayed similar vertical structure as those observed along the 2005/2006 CORSACS expeditions;
537 however, the CICLOPS dCo and labile dCo concentrations were notably lower throughout the
538 water column compared to the CORSACS datasets (Fig. 8). This trend was particularly clear in
539 the Ross Sea, where the stations from both expeditions contained the greatest regional overlap
540 (Fig. A1) and labile dCo distributions from the prior 2006 CORSACS-2 expedition exceeded those
541 observed on the 2017/2018 CICLOPS expedition (Fig. 9a-c; Table 4). The CORSACS-1 and
542 CORSACS-2 expeditions displayed average deep ($\geq$ 100 m) dCo concentrations of 55 ± 4 pM and
543 56 ± 6 pM, respectively, and CORSACS-2 displayed average deep labile dCo concentrations of
544 21 ± 7 pM; on CICLOPS, in contrast, the Ross Sea displayed average deep dCo and labile dCo
545 concentrations of 46 ± 8 pM and 9 ± 7 pM, respectively. Note that the CICLOPS expedition mean
546 deep dCo inventory displayed a higher standard deviation (8 pM) compared to the CORSACS-1
547 (4 pM) and CORSACS-2 (6 pM) expeditions, indicating a higher variability of deep dCo
548 concentration within the sites and depths sampled; no difference in standard deviation was
549 observed within the deep labile dCo inventories of the CICLOPS and CORSACS-2 expeditions
550 (both 7 pM). Independent t-tests determined that CORSACS-1 and CORSACS-2 deep Ross Sea
551 dCo values were statistically similar ($p = 0.27$) while deep CICLOPS dCo values were statistically
552 different from CORSACS-1 and CORSACS-2 deep dCo ($p < 0.0001$; Table 4). This offset
553 represents a mean dCo inventory loss of $8 - 10$ pM dCo in the deep ocean, and approximately all
554 of the difference can be accounted for by the loss of deep labile dCo (12 pM dCo; Fig. 9d-g), the
555 more bioavailable form of dCo for biological uptake. Since a plot of temperature vs. salinity shows
556 largely overlapping hydrography among the three expeditions in the Ross Sea (Fig. A2), the
557 observed difference in dCo inventories is unlikely to be due to differences in the distributions of
558 the water masses sampled.

559   In the near-surface (10 m), labile dCo was undetectable at 3 of the 4 stations in the Ross
560 Sea on CICLOPS, and the near-surface labile : total dCo ratio in the one station where labile dCo
561 was detectable (station 29; 3.5 pM labile dCo) was only 0.09. In contrast, the 2006 CORSACS-2
562 expedition reported the presence of labile dCo at five stations with concentrations of 17 ± 7 pM at
563 6 m depth and 14 ± 9 pM at 16 m depth, with reported labile : total dCo ratios of 0.37 ± 0.13 and
564 0.28 ± 0.17, respectively. This trend can be at least partially explained by the seasonality
565 differences between the spring CORSACS-2 expedition and the summer CICLOPS expedition; as
566 the phytoplankton bloom progresses in the photic zone of the Ross Sea, labile dCo concentrations
567 would be drawn down by community uptake and would exhibit lower concentrations later in the
568 summer season. This seasonal trend was evident in the surface dCo inventory differences between
569 the summer CORSACS-1 and spring CORSACS-2 expeditions (Fig. 9a,d,e). However, the low,
570 often undetectable, labile dCo concentrations observed in the surface Ross Sea on the CICLOPS

expedition illustrate the intensity of bloom-driven labile dCo depletion in the region, leaving 91–
100% strong ligand-bound dCo in the surface Ross Sea. These observations are consistent with
the Co uptake rate measurements, which were found to be higher on CICLOPS (0.84 pM d^{-1}, n =
38) compared to CORSACS-1 and CORSACS-2 (0.67 pM d^{-1} and 0.25 pM d^{-1}, respectively) (Saito
et al., 2010; Rao, 2020).
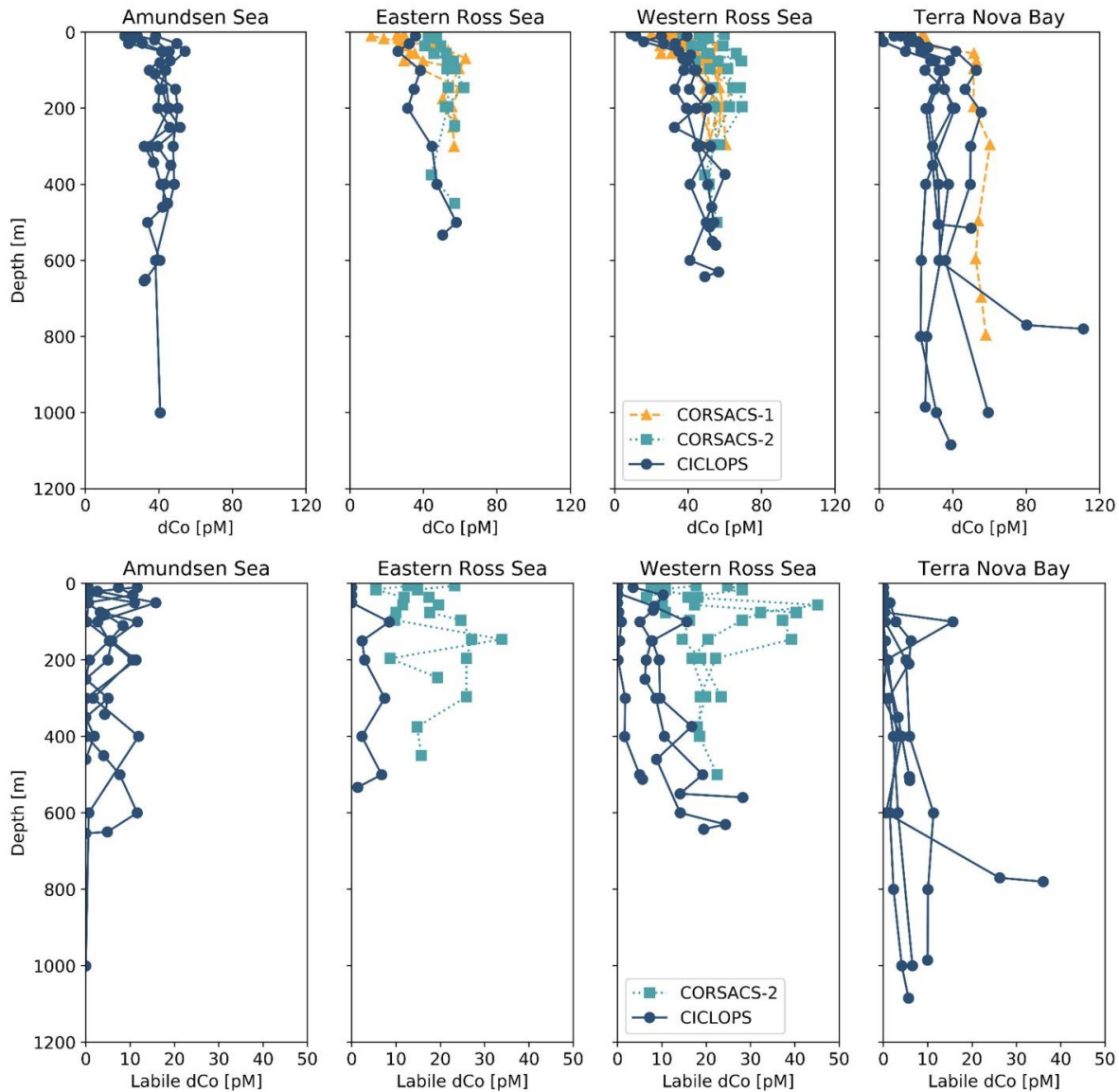
Figure 8. Dissolved Co and labile dCo depth profiles from the CORSACS-1 (NBP0601;
December 27, 2005 – January 23, 2006), CORSACS-2 (NBP0608; November 8, 2006 – December
3, 2006) and CICLOPS (NBP-1801; December 11, 2017 – March 3, 2018) expeditions in the 4
regions sampled by the CICLOPS expedition: Terra Nova Bay, the Western Ross Sea, the Eastern
Ross Sea and the Amundsen Sea. The Eastern and Western Ross Sea stations are defined by being
either east or west of the 175 ºE longitudinal, respectively. The CORSACS expeditions did not
extend to the Amundsen Sea, and no labile dCo was reported from the CORSACS-1 expedition.
dCo data from the CORSACS expeditions was reported in Saito et al. (2010) and is accessible at
https://www.bco-dmo.org/dataset/3367.
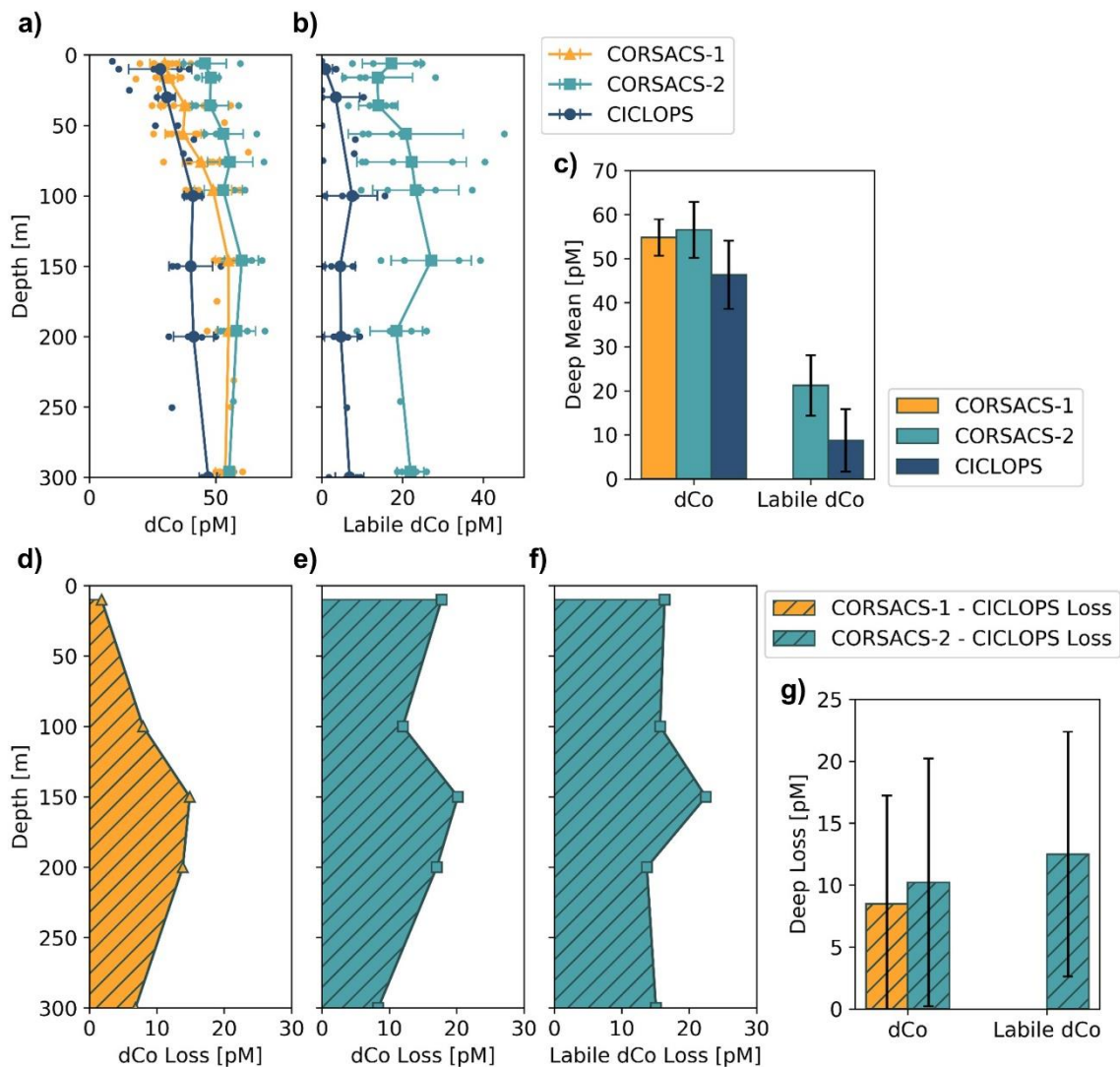
Figure 9. Mean depth profiles of dCo **(a)** and labile dCo **(b)** from the Ross Sea from three sampling seasons, including the expeditions: CORSACS-1 (Summer 2005/2006), CORSACS-2 (Spring 2006) and CICLOPS (Summer 2017/2018). Observed profile values are plotted as unconnected dots, and the mean profile is plotted for each depth at which at least three samples were analyzed. **(c)** The mean deep (≥ 100 m) dCo and labile dCo concentrations for stations in the Ross Sea on each expedition. The mean difference in the dCo **(d, e)** and labile dCo **(f)** profiles between the CORSACS and CICLOPS expeditions where sample depths were within 5 m of each other. **(g)** The mean deep (≥ 100 m) dCo and labile dCo concentration loss for stations in the Ross Sea. Error bars denote one standard deviation from the mean. No labile dCo data is available for the CORSACS-1 expedition. Mean values, loss values, and the results of independent t-tests to determine the significance of the deep dCo loss are given in Table 4.

Dissolved Co and labile dCo concentrations were also analyzed in the Ross Sea in 2009 by sampling the water column below the McMurdo Sound seasonal sea ice in the early spring (November 9–23) (Noble et al., 2013). Under the ice, the water column was well-mixed, and the dCo and labile dCo profiles showed relative uniformity at all three stations measured (Fig. 2 of

Noble et al., 2013). In the deep ocean (≥ 100 m), the mean dCo and labile dCo concentrations were 51 ± 4 and 15 ± 2 pM, respectively, which is lower than those observed on the 2005/2006 CORSACS expeditions and higher than those observed on the 2017/2018 CICLOPS expedition (Table 4). The mean deep labile dCo concentrations from the McMurdo Sound fieldwork were also significantly different from the mean deep labile dCo observed on CICLOPS ($p = 0.0006$), displaying an average deep labile dCo difference of 6 pM. This dataset supports the possibility of a long-term trend towards a decreasing deep dCo inventory in the Ross Sea, although the more coastal location and difference in sea ice cover should be considered when comparing the McMurdo Sound dataset to the CORSACS and CICLOPS observations. Notably, the methodology and instrumentation used to measure both dCo and labile dCo on both CORSACS expeditions, the McMurdo Sound fieldwork and the CICLOPS expedition were functionally identical, with the exception of an autosampler (Metrohm 858 Sample Processor) used on the 2017/2018 CICLOPS expedition.

Table 4. The mean dCo and labile dCo observed in the deep (≥ 100 m) Ross Sea, and the average deep dCo loss between 3 previous sampling expeditions (CORSACS-1 in summer 2005/2006; CORSACS-2 in spring 2006; under-ice sampling in McMurdo Sound in spring 2009) and the CICLOPS expedition (2017/2018). Dissolved Co and labile dCo loss values were calculated as the difference between mean deep concentrations observed on previous expeditions and those observed on the CICLOPS expedition. No labile dCo data (n.d.) is presented from the CORSACS-1 expedition. Independent t-tests were performed to determine the significance of difference between the deep mean concentrations from previous expeditions compared to the CICLOPS expedition; * indicates a significant difference between CICLOPS and a previous expedition ($p < 0.005$). The mean deep dCo concentrations from the CORSACS expeditions were not significantly different from each other ($p = 0.27$).

	dCo$_{mean}$ [pM]	n	Labile dCo$_{mean}$ [pM]	n	dCo Loss [pM]	p-value	Labile dCo Loss [pM]	p-value
CORSACS-1[a]	55 ± 4	26	n.d.		8 ± 9	< 0.0001*	--	--
CORSACS-2[a]	56 ± 6	19	21 ± 7	20	10 ± 10	< 0.0001*	12 ± 10	< 0.0001*
McMurdo Sound[b]	51 ± 4	19	15 ± 2	19	4 ± 8	0.02	6 ± 7	0.0006*
CICLOPS	46 ± 8	32	9 ± 7	32	--	--	--	--

[a] Data originally published in Saito et al. (2010).
[b] Data originally published in Noble et al. (2013).

The low labile dCo inventory in the Ross Sea was a surprising discovery during CICLOPS since relatively high concentrations of labile dCo were previously noted to be a distinctive feature of the Ross Sea and Southern Ocean when compared to the tropical and subtropical global oceans (Saito et al., 2010). In prior studies in this region, high labile : total dCo ratios were hypothesized to be due to the absence of ligand-producing – and vitamin B_{12}-producing – marine cyanobacteria like *Synechococcus* in the Ross Sea (Caron et al., 2000; DiTullio et al., 2003; Bertrand et al., 2007), since *Synechococcus*-dominated communities have been known to produce a substantial amount of Co ligands (Saito et al., 2005). However, high Co ligand concentrations and low labile dCo concentrations have previously been observed at a more pelagic location in the Southern Ocean

638 near New Zealand, where it was hypothesized that the decay of a eukaryotic phytoplankton bloom
639 generated higher abundances of Co-binding ligands in the surface ocean (Ellwood et al., 2005).

640   The decrease in the dCo and labile dCo inventories was apparent when the CICLOPS and
641 CORSACS dCo vs. dPO_4^{3-} relationships across all expedition regions were compared (Fig. 6c,e).
642 Over similar dPO_4^{3-} ranges, the CICLOPS dCo concentrations are generally lower than those
643 observed on CORSACS, and the CICLOPS labile dCo concentrations are considerably lower, with
644 labile dCo essentially absent from upper ocean samples with a dPO_4^{3-} concentration < 1.75 µM.
645 Despite the lack of observable scavenging, the CICLOPS dCo vs. dPO_4^{3-} relationship appeared to
646 be noticeably nonlinear throughout the water column ($R^2 = 0.42$), while CORSACS samples
647 displayed a more linear trend ($R^2 = 0.57$). The CICLOPS dCo vs. dPO_4^{3-} relationship creates a
648 concave, "scooped" shape where dCo was depleted relative to dPO_4^{3-}, displaying a lower slope in
649 the upper ocean than was observed on the CORSACS expeditions (Fig. 6c). This scooped shape
650 was particularly evident in Terra Nova Bay where the upper ocean dCo : dPO_4^{3-} stoichiometric
651 slope was the lowest (26 ± 4 µmol : mol; $R^2 = 0.65$). The depletion of dCo relative to dPO_4^{3-}
652 observed on CICLOPS appears driven by the shift in Co speciation as a result of near-total uptake
653 of the upper ocean labile dCo fraction and subsequent dominance of the remaining strong ligand-
654 bound dCo fraction in the upper ocean. Similar to the deep dCo loss described above, the difference
655 between the CORSACS and CICLOPS dCo vs. dPO_4^{3-} relationship can be accounted for by the
656 depletion of the labile dCo inventory. In the deep ocean where both dCo and dPO_4^{3-} are more
657 abundant, the large range in dCo concentrations relative to dPO_4^{3-} concentrations may be evidence
658 of deep inputs of dCo and labile dCo from the nepheloid layer, which was more attentively sampled
659 on CICLOPS than either CORSACS expedition (Sect. 4.1).

660 4.4 Dissolved Co, Zn and Cd stoichiometry

661   Dissolved Zn concentrations observed on CICLOPS were low in the surface ocean,
662 particularly in Terra Nova Bay, where dZn concentrations in the sub-nanomolar ranges were
663 observed (average dZn = 0.87 ± 0.42 at 10 m depth, n = 11). Marine microbes require Zn for a
664 wide range of metabolic uses; for example, eukaryotic phytoplankton use Zn as a cofactor in
665 carbonic anhydrase (Roberts et al., 1997; Morel et al., 2020) and bacteria such as
666 *Pseudoalteromonas* use Zn in a range of proteases (Mazzotta et al., 2021). Prior culture studies
667 have found that Zn scarcity can lead to co-limitation of both Zn and carbon in several eukaryotic
668 phytoplankton strains (Morel et al., 1994; Sunda and Huntsman, 2000), and field incubation
669 experiments have shown evidence for Zn co-limitation with Fe (Jakuba et al., 2012) and silicate
670 (Chappell et al., 2016) in the Pacific Ocean. During the CICLOPS expedition, an incubation
671 experiment performed at Station 27 in Terra Nova Bay found compelling evidence for Zn and Fe
672 co-limitation, which constrained Chl-a production and DIC draw-down by phytoplankton in the
673 region (Kellogg et al., [Submitted]).

674   Many but not all phytoplankton are able to substitute Co and Cd for Zn as their carbonic
675 anhydrase metallic cofactor (Lee and Morel, 1995; Sunda and Huntsman, 1995; Lane et al., 2005;
676 Kellogg et al., 2022), which provides metabolic flexibility and a competitive edge in low-dZn
677 environments (Kellogg et al., 2020). The Cd-containing carbonic anhydrase CDCA is currently
678 the only known metabolic use of Cd, and the uptake of dCd and dCo in the photic zone, both metals
679 which are typically less abundant than dZn in the oceans, often increases under low dZn conditions
680 (Sunda and Huntsman, 1995, 1996; Jakuba et al., 2008; Kellogg et al., 2020; Morel et al., 2020).
681 Cations like Zn, Cd and Co that possess similar charge and atomic radii often share the same

682   transporter uptake systems, and the relative availability of different metal cofactors for use in an
683   organism's metalloproteome is partially determined by the environmental metal concentrations
684   and the affinity of the metals for ligands associated with a cell's metal transport proteins (Irving
685   and Williams, 1948; Sunda and Huntsman, 1992, 1995). When dZn concentrations are low, more
686   Cd and Co are able to bind to the transporter ligands despite the relative stability of their ligand-
687   bound complexes, which tend to be lower for Co than for Zn. Through this mechanism, dZn
688   concentrations and cycling can influence the distribution and uptake of Co and Cd, particularly in
689   low dZn environments like the Ross Sea and Terra Nova Bay.

690   The dZn vs. dPO_4^{3-} and dCd vs. dPO_4^{3-} relationships observed in the Amundsen Sea, Ross
691   Sea and Terra Nova Bay were compared relative to dCo vs. dPO_4^{3-} (Fig. 7; Table 3). For this
692   analysis, the depth threshold that separates the upper ocean from the deep ocean was selected
693   manually in order to optimize the linear fit of the upper and deep ocean trends and to best capture
694   the depth dependence of the observed trace metal stoichiometries. This depth threshold can best
695   be conceptualized as an inflection point that represents the largest change in trace metal
696   concentrations with respect to depth or, in this case, dPO_4^{3-} concentration. The depth threshold
697   used for dCo in both the Ross Sea and Terra Nova Bay (100 m) is deeper than those used for dZn
698   and dCd, (range of 25 – 50 m). Thus, the inflection points of the "scoops" in the trace metal
699   stoichiometries are driven by the uptake stoichiometry of the region's phytoplankton community
700   rather than the mixed layer depth of the upper ocean. The shapes observed in the dZn vs. dPO_4^{3-}
701   and dCd vs. dPO_4^{3-} relationships were similar to that of dCo vs. dPO_4^{3-}, exhibiting distinct
702   differences in slope between surface and deep waters. The stark difference in trace metal
703   stoichiometry slopes between the upper and deep ocean is likely driven by differences in metal
704   speciation over depth. In the surface ocean, a shallower trace metal : dPO_4^{3-} slope suggests a trace
705   metal fraction that is largely bound to strong organic ligands, with a smaller excess labile fraction.
706   The more bioavailable labile fraction of metals would have been drawn down by phytoplankton,
707   whose uptake transport systems preferentially bind to labile metals. At deeper depths, the presence
708   of labile metals in excess of strong organic ligands results in a higher metal : dPO_4^{3-} slope.

709   A shallow dCo : dPO_4^{3-} slope that extends below the photic zone could suggest Co uptake
710   by heterotrophic bacteria, archaea and possibly sinking phytoplankton below the photic zone.
711   Heterotrophic prokaryotic uptake of labile Co is largely driven by the bacteria and archaea that
712   contain a vitamin B_{12} synthesis pathway that is absent in all eukaryotes (Warren et al., 2002;
713   Osman et al., 2021); unlike carbonic anhydrase, the use of Co as a co-factor in the vitamin B_{12}
714   corrin ring structure cannot be substituted for by other divalent cations like Zn and Cd. Many
715   vitamin B_{12}-synthesizing bacteria possess genes for Co(II)-specific transporters in addition to more
716   general metal ion transporters, and the Co-specific transporters are regulated by cellular
717   concentrations of vitamin B_{12}, illustrating the importance of vitamin B_{12} synthesis in driving
718   bacterial Co uptake (Osman et al., 2021); however, this mechanism has not been observed within
719   marine bacterial communities. Additionally, vitamin B_{12} uptake by both prokaryotes and
720   eukaryotes has been found to be common in Antarctic coastal communities (Taylor and Sullivan,
721   2008; Rao, 2020), and likely contributes to the depletion of ligand-bound dCo in both the surface
722   and mesopelagic ocean.

723   The shallower Zn apparent nutricline could also be explained by the higher stability of Zn
724   metal-ligand complexes compared to Co complexes within phytoplankton metabolisms, allowing
725   higher uptake rates of dZn when available (Irving and Williams, 1948; Sunda and Huntsman,
726   1995). The vertical dimension of trace metal loss captured by a comparison of these apparent

727 nutriclines could be conceptualized as a time-dependent process driven by the phytoplankton
728 community's preference for each trace metal, with preferred nutrients like Zn exhibiting a
729 shallower stoichiometric inflection point arising from the rapid depletion of the metal within the
730 photic zone, and nutrients like dCo, which is often taken up by eukaryotes when dZn is scarce
731 (Sunda and Huntsman, 1995; Kellogg et al., 2020), exhibiting a deeper stoichiometric inflection
732 point below the photic zone. This analysis suggests that substitution at the interface of the uptake
733 mechanism for trace metal transporters at least partially controlled the stoichiometry of Zn/Cd/Co
734 distributions and uptake in the upper ocean.

735 4.5 Zn/Cd/Co uptake using a shared trace metal membrane transport system

736   This study synthesized dissolved concentration and uptake datasets for Co, Zn and Cd
737 (Table 5), three trace metal nutrients whose use by phytoplankton is collectively integral to surface
738 ocean productivity and the biogeochemical cycling of Fe, vitamin B_{12} and carbon in the Southern
739 Ocean. This combined dataset is ideal for interrogating questions of environmental competitive
740 inhibition of Zn, Cd and Co transport in low-dZn environments. The observation of order of
741 magnitude trends in trace metal uptake rates over depth profiles ($\rho Zn > \rho Cd > \rho Co$) was novel,
742 and paralleled the order of magnitude trends of trace metal concentrations in seawater ([Zn] > [Cd]
743 > [Co]; Fig 5). This environmental observation reflected the findings of numerous culture
744 experiments that quantify the uptake of trace metals as a function of the concentration of available
745 labile metals and the affinity of the metal for a cell transporter's binding ligand (Irving and
746 Williams, 1948; Sunda and Huntsman, 1992, 1995, 2000; Kellogg et al., 2020).

747   Evidence for elevated Co uptake in the low-dZn environments of the surface ocean were
748 supported by the trace metal uptake rates. When ρZn and ρCd was normalized to ρCo ($\rho M : \rho Co$;
749 Fig. 5), deviations from these order-of-magnitude trends were observed. In particular, at Stations
750 4 and 11 in the Amundsen Sea and Station 22 in Terra Nova Bay, ρZn and ρCd stoichiometry
751 relative to ρCo tended to decrease towards the surface in the upper 50 m, while the opposite trend
752 appeared to occur at Station 57 in the late summer. The surface-most trends of stations 20 and 57
753 were undetermined due to a lack of a 10 m ρCo value. This increasing surface Co uptake
754 stoichiometry relative to Zn and Cd at Stations 4, 11 and 22 – stations that also displayed
755 significant phytoplankton blooms – suggests that Co uptake increased in low-Zn environments,
756 while later in the summer at Station 57, ρCo lessened relative to ρZn, possibly due to the deepening
757 of the mixed layer in February, bringing additional dZn to the upper ocean via vertical mixing
758 (Fig. 4). The increase in the observed ρCo rate was likely due to the upregulation of the shared Zn
759 and Co uptake transporter system. From laboratory culture experiments aimed at examining the
760 microbial uptake of Zn and other trace metals, it is apparent that many diatoms and
761 coccolithophores contain two distinct Zn uptake systems: a low-affinity system that operates at
762 higher concentrations of dZn and a high-affinity system that functions at lower concentrations of
763 dZn (Sunda and Huntsman, 1992; John et al., 2007). Both transport mechanisms are relatively
764 unspecific as to the divalent metals transported into the cell; the low-affinity system is known to
765 transport Zn, Cd and Mn, while the high-affinity system transports Zn, Cd and Co. (Sunda and
766 Huntsman, 1995, 1996); thus, Co uptake is often inhibited at high dZn concentrations when the
767 low-affinity system is active (Sunda and Huntsman, 1995; Sunda 2012). In culture, diatoms have
768 been observed to switch from the low-affinity to the high-affinity transport system between $10^{-10.5}$
769 and $10^{-9.5}$ M dZn^{2+} (Sunda and Huntsman, 1992; John et al., 2007), a relevant range for the lowest
770 values of total dZn observed in the surface ocean on CICLOPS (dZn minimum = 1×10^{-10} M at

771 Station 46, 10 m depth), and the dZn^{2+} pool would have been even smaller due to organic
772 complexation.

773 **Table 5.** Dissolved stoichiometric ratios and uptake stoichiometric ratios of five station profiles
774 for Co, Cd and Zn. The dCo : dCd : dZn : dPO$_4^{3-}$ ratio is the dissolved stoichiometry of metals
775 present in the water column normalized to dPO$_4^{3-}$, and the ρCo : ρCd : ρZn ratio is the uptake
776 stoichiometry of microbial communities normalized to ρCo.

777

Region	Station	Depth [m]	dCo : dCd : dZn : dPO$_4^{3-}$	ρ Co : ρ Cd : ρ Zn
Amundsen Sea	4	10	19 : 314 : 1,716 : 1,000,000	1 : 8 : 56
		30	23 : 295 : 1,889 : 1,000,000	1 : 16 : 88
		50	24 : 293 : 2,096 : 1,000,000	1 : 15 : 108
	11	10	13 : 204 : 1,018 : 1,000,000	1 : 10 : 77
		20	15 : 212 : 970 : 1,000,000	1 : 13 : 89
		30	17 : 231 : 1,290 : 1,000,000	1 : 29 : 294
		50	19 : 280 : 1,835 : 1,000,000	1 : 0*: 229
		75	21 : 301 : 2,009 : 1,000,000	1 : 0* : 532
		100	23 : 358 : 2,727 : 1,000,000	1 : 11 : 708
		150	17 : 313 : 1,974 : 1,000,000	1 : 0* : 797
		200	17 : 325 : 2,137 : 1,000,000	1 : 3 : 885
Ross Sea	20	30	17 : 323 : 1,846 : 1,000,000	1 : 13 : 349
		50	13 : 305 : 2,020 : 1,000,000	1 : 11 : 163
		100	17 : 333 : 2,400 : 1,000,000	1 : 0* : 376
		150	16 : 330 : 2,321 : 1,000,000	1 : 0* : 507
		200	14 : 336 : 2,358 : 1,000,000	1 : 0* : 913
Terra Nova Bay	22	10	15 : 136 : 617 : 1,000,000	1 : 12 : 81
		25	10 : 158 : 546 : 1,000,000	1 : 11 : 75
		40	11 : 254 : 1,127 : 1,000,000	1 : 29 : 166
		75	13 : 301 : 1,965 : 1,000,000	1 : 7 : 228
		100	11 : 304 : 1,938 : 1,000,000	1 : 56 : 705
		150	16 : 310 : 2,212 : 1,000,000	1 : 122 : 584
	57	50	13 : 179 : 894 : 1,000,000	1 : 17 : 37
		75	13 : 297 : 1,644 : 1,000,000	1 : 3 : 18
		100	15 : 320 : 1,798 : 1,000,000	1 : 8 : 40

778
779 *Denotes depths at which ρCd was under the methodological detection limit.

780   To investigate the influence of transporter competitive inhibition on trace metal uptake via
781 the high-affinity uptake system, we can estimate the predicted ρCo, ρCd and ρZn values given the
782 observed trace metal concentrations with an equation adapted from Michaelis-Menten enzyme-
783 substrate kinetics (Sunda and Huntsman, 1996, 2000):

784
$$\text{Predicted } \rho M = \frac{V_{max}[M^{2+}]K_M}{[Co^{2+}]K_{Co} + [Cd^{2+}]K_{Cd} + [Zn^{2+}]K_{Zn}}$$

785 where M is the trace metal (Co, Cd, Zn) whose uptake is being calculated, V_{max} is the saturation
786 uptake rate of the transporter system, and K_{Co}, K_{Cd} and K_{Zn} are steady state affinity constants for

787 the metal-ligand complex associated with the membrane transporter. For this system, we assumed
788 $K_{Zn} = K_{Cd} = K_{Co} = 10^{9.6}$, where $10^{9.6}$ is the value of K_{Zn} for the high-affinity uptake system
789 determined by Sunda et al. (1992), and that 99% of the dCo, dCd and dZn inventory was bound to
790 strong organic ligands, leaving 1% of the total metal concentration labile. Note that the assumption
791 that K and the percent labile multipliers are equal for all metals results in their value being nullified
792 by their presence in both the numerator and denominator of the predicted uptake equation, and so
793 their assumed values have no numerical impact on the predicted uptake values. It was also assumed
794 that V_{max} values for each trace metal were equal, which is likely a reasonable assumption for metals
795 that share an uptake system, although V_{max} is known to vary with trace metal concentration, a
796 function that we have assumed here to be negligible (Sunda and Huntsman, 1985, 1996; Sunda,
797 1989). V_{max} is in units of μmol (mol C)$^{-1}$ d^{-1}, and the predicted trace metal uptake rates were
798 converted to units of M d^{-1} using a C : Chl-a ratio of 130 w/w, derived from the Ross Sea
799 phytoplankton community (DiTullio and Smith, 1996).

800   When the predicted metal uptake rates were calculated using a V_{max} value of 262 μmol (mol
801 C)$^{-1}$ d^{-1} from previous Zn culturing experiments (Sunda and Huntsman, 1992), the resulting values
802 recreated the trend of the observed trace metal uptake profiles, with higher uptake rates in the
803 surface ocean and lower rates below the photic zone, but the predicted values were over an order
804 of magnitude greater than the measured uptake rates (Fig. B1). This offset may be due to several
805 factors: (1) the assumed C : Chl-a ratio to scale predicted uptake with observed biomass may be
806 high, (2) the V_{max} value calculated from laboratory experiments may be high, or (3) the
807 assumptions that the speciation of the dissolved trace metals are 99% strongly-bound at all depths,
808 for all metals is incorrect. The final explanation may play a role in the offset between the predicted
809 and observed uptake rates, and illustrates the complexities of translating lab-based culture work to
810 environmental measurements and in-situ analyses. The V_{max} value is also relatively unconstrained,
811 and it is reasonable to assume it may be lower in the Ross Sea than observed in culture if the
812 phytoplankton exhibit suppressed metal quotas to survive in a metal-deplete environment. With
813 this in mind, the V_{max} value was tuned to 4 μmol (mol C)$^{-1}$ d^{-1} to fit the observed uptake rates,
814 which is lower than any Co, Cd or Zn V_{max} reported in the literature from culture studies (Fig. 10).
815 Using the tuned V_{max} value, the high-affinity uptake system equation properly predicts the order
816 of magnitude trends inherent in the observed Co/Cd/Zn uptake rates. This analysis demonstrates
817 the measured uptake rates from the Ross Sea were likely driven by the concentration ratios of
818 available metals throughout the water column, following a high-affinity transporter model of Co,
819 Cd and Zn uptake.

820   The maximum diffusive limit, a calculation of the phytoplankton community's maximum
821 diffusion rate for the uptake of trace metal nutrients through their cell membranes, was also
822 estimated and compared to the observed and predicted uptake rate profiles. The physical limits of
823 uptake via diffusion was determined as a function of the surface area of phytoplankton membranes
824 (Sunda and Huntsman, 1992):

825 $$\text{Maximum diffusive limit} = 4\pi r D [M^{2+}]$$

826 where r is the equivalent spherical radius of a phytoplankton cell, assumed to be 3 μm, a reasonable
827 value for diatom species, and D is a diffusion rate constant of 2 x 10^{-6} cm^2 s^{-1}, calculated for Zn^{2+}
828 at 20⁰C (Sunda and Huntsman, 1992). The diffusive limit was converted to units of M d^{-1} using a
829 C : cell volume ratio of 12.5 mol C L^{-1}, which is the average of two diatom ratios reported in Sunda
830 and Huntsman (1995) (11 and 14 mol C L^{-1}), and the same C : Chl-a ratio of 130 w/w used for the
831 predicted uptake rate estimate above (DiTullio and Smith, 1996). The resulting diffusive limit

832 profiles are highly dependent on the assumed speciation of each trace metal; when the dCo, dCd
833 and dZn inventories were assumed to be 99% bound (Fig. 10), the maximum diffusive limit was
834 slightly greater than the predicted and observed uptake rates, but when the inventories were
835 assumed to be 100% labile (Fig. B1), the diffusive limit greatly exceeded the uptake rates by
836 several orders of magnitude. Since the metal inventories almost certainly vary in their speciation
837 of dZn and dCd over depth, as was observed in the dCo inventory, an accurate maximum diffusive
838 limit would exist between the two extremes of 0% bound and 99% bound, and might be expected
839 to be greater at deeper depths, where a higher fraction of the dissolved metal inventory is labile.
840 For additional analysis of the predicted metal uptake ratios and the maximum diffusive limit, see
841 Appendix B.
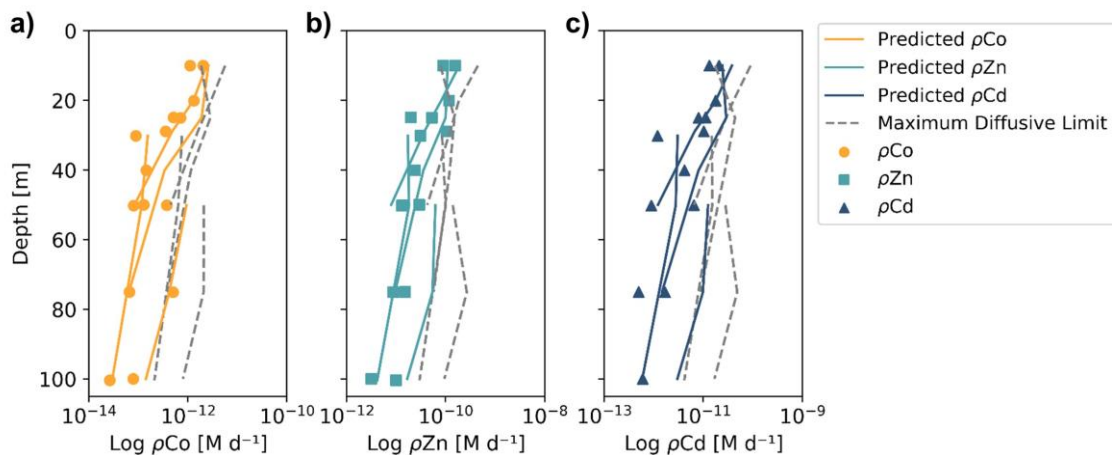
842
843 **Figure 10.** Observed (markers) and predicted (solid lines) trace metal uptake rate (ρ) profiles for
844 Co **(a)** Zn **(b)** and Cd **(c)** from Stations 11, 20, 22 and 57. The maximum diffusive limit profiles
845 (dashed lines) are shown as an estimate of the physical limits of metal diffusion through uptake
846 transporters. The predicted uptake rates were tuned to best fit the observed uptake rate trends by
847 using a V_{max} value of 4 µmol (mol C^{-1}) d^{-1}, and the maximum diffusion limit estimation assumed
848 a speciation of 1% labile metals.

849 4.6 Vitamin B$_{12}$ and Zn stress, and their implications for increasing biological dCo demand

850   The near-absence of labile dCo and low concentration of ligand-bound dCo in coastal
851 Antarctic seas may indicate a larger shift in the region towards vitamin B$_{12}$ limitation. Vitamin B$_{12}$
852 has been shown to be co-limiting with Fe in the Ross Sea and elsewhere (Sañudo-Wilhelmy et al.,
853 2006; Bertrand et al., 2007), and increased vitamin B$_{12}$ uptake by both bacterioplankton and
854 eukaryotic phytoplankton has been observed in incubation experiments following the alleviation
855 of surface ocean Fe limitation (Bertrand et al., 2011). Two primary sources of Fe to the Antarctic
856 seas are a flux of lithogenic Fe from melting ice shelves along the continent and sediment
857 resuspension along the seafloor, both of which have been observed to be meaningful Fe sources to
858 the Amundsen Sea (Planquette et al., 2013; St-Laurent et al., 2017). The source of particulate Fe
859 from glacial meltwater to coastal Antarctic seas has been increasing over the past several decades
860 and is expected to continue to increase as Antarctic ice shelves and glaciers melt and retreat due
861 to global climate change (Monien et al., 2017). The source of particulate Co from glacial meltwater
862 would also be expected to increase since Co, like Fe, has been observed to be transported from the
863 Antarctic continent via ice melt (Westerlund and Öhman, 1991), and it is unclear what role this

864 presumably increasing source of Co to the surface ocean plays in the reduced inventories of dCo
865 in the surface ocean.

866   Although it is difficult to definitively conclude that the low dCo inventory observed on
867 CICLOPS is representative of a decadal trend towards vitamin B_{12} limitation and not simply
868 variation in micronutrient availability and community structure, the inventory and stoichiometric
869 uptake trends documented in this study are compelling evidence for a changing biogeochemical
870 Co cycle in the coastal Southern Ocean. Paired with the recent discovery of Zn/Fe co-limitation in
871 Terra Nova Bay (Kellogg et al., [Submitted]), these results suggest a complex landscape of
872 micronutrient scarcity and limitation in coastal Antarctic seas where plankton community
873 structures and Fe additions from melting ice sheets can generate patches of vitamin B_{12} and Zn
874 limitation within a broadly Fe-scarce HNLC region.

875   The bacterial community is essential to the development and alleviation of vitamin B_{12}
876 limitation within a eukaryotic phytoplankton bloom since only prokaryotes possess the metabolic
877 pathway to synthesize the vitamin (Warren et al., 2002; Croft et al., 2005). In the Southern Ocean,
878 near-zero counts of photosynthetic bacteria indicate that the heterotrophic bacterial communities
879 are primarily responsible for vitamin B_{12} production in the region (Bertrand et al., 2011). Vitamin
880 B_{12} can become limiting when the bacterial community is low in abundance and/or growth limited
881 by a different nutrient such as dissolved organic matter (DOM). In the Ross Sea, bacterioplankton
882 have been found to be growth limited by an inadequate supply of DOM (Church et al., 2000;
883 Bertrand et al., 2011), and there can be up to a one-month lag between the onset of the spring
884 phytoplankton bloom and an associated bacterial bloom stimulated by phytoplankton DOM
885 production (Ducklow et al., 2001). This offset suggests that vitamin B_{12} limitation among
886 eukaryotes is most probable earlier in the season within the spring bloom. Additionally, low
887 abundances of mesozooplankton and microzooplankton grazing rates in the Ross Sea create
888 phytoplankton blooms with low grazing pressure (Caron et al., 2000; Ducklow et al., 2001), which
889 may allow low DOM conditions to persist later into a bloom and exacerbate vitamin B_{12} stress
890 among eukaryotes.

891   A shift towards vitamin B_{12} limitation would likely favor phytoplankton with flexible
892 metabolisms that are able to reduce their demand for Co and vitamin B_{12} when necessary.
893 Organisms that can express the vitamin B_{12}-independent *metE* gene may out-compete those
894 expressing the vitamin B_{12}-dependent *metH* gene (Rao et al., [In review]; Rodionov et al., 2003;
895 Bertrand et al., 2013; Helliwell 2017). *P. antarctica*, for example, may be well suited to periods
896 of vitamin B_{12} limitation due to the symbiotic bacterial microbiomes that form within its colonies
897 and produce B vitamins that allow the colonies to grow when B vitamins are otherwise unavailable
898 (Brisbin et al., 2022). *P. antacrica* has also been found to express a novel *metE*-fusion gene when
899 vitamin B_{12} limited and *metH* gene while vitamin-replete, suggesting a highly flexible vitamin B_{12}
900 metabolism (Rao et al., [In review]).

901   There is compelling evidence for high rates of biological Co uptake in the Ross Sea during
902 the 2017/2018 summer compared to the 2005/2006 summer driven by the uptake of dCo from
903 vitamin B_{12} and Zn scarcity. Together, these two stressors increase the rate of Co uptake as well
904 as the Co : C stoichiometry of phytoplankton biomass. The stoichiometry of Co uptake has been
905 observed to be highly plastic in this study and others, responding to the availability of other
906 micronutrients and the requirements of the microbial community (Sunda and Huntsman, 1995;
907 Saito et al., 2017). An increase in ρCo could then result in a decrease of the Co inventory in coastal
908 Antarctic seas, following the mechanism detailed below.

909   Biological uptake alone would not permanently remove Co from the water column; uptake
910 only shifts Co from the dissolved phase to the particulate phase, where POM remineralization
911 restores Co back to the dissolved phase. The net removal pathways of Co include (1) burial as
912 POM, (2) particle scavenging and (3) depletion of dCo into Circumpolar Deep Water (CDW) and
913 Antarctic Bottom Water (ABW). We have already noted that Co scavenging to Mn-oxides is
914 particularly low in the Southern Ocean (Oldham et al., 2021). The advection of dCo into CDW
915 may not be at a steady state throughout the year since cycles of ice melt and formation affect the
916 mixing of CDW and formation of dense Antarctic Bottom Water (ABW), and so may represent a
917 removal pathway for dCo on an annual cycle. However, an increase in the burial flux of Co in
918 POM is the most likely pathway for sustained loss of the Co inventory. When the ρCo rate
919 increases, the stoichiometry of Co incorporation into biomass relative to P would also increase.
920 Over the years, a strengthened demand for Co via vitamin B_{12} and Zn stress could result in a steady
921 loss of Co if the Co : C and Co : PO_4^{3-} stoichiometry of POM increases but the remineralization of
922 POM is unchanged, increasing the flux of particulate Co into the deep ocean and sediments. In the
923 winter, sea ice covers the Antarctic seas and the water column mixes, a process that would
924 propagate the low dCo concentrations from the photic zone into the deep ocean and result in a
925 steady loss of the dCo inventory throughout the water column.

926   Additionally, warming surface ocean temperatures likely play a role in phytoplankton
927 productivity and nutrient uptake. Increasing both dFe availability and temperature have been
928 shown to significantly increase phytoplankton growth and phytoplankton abundance in the Ross
929 Sea, and impact community structure (Rose et al., 2009; Spackeen et al., 2018; Zhu et al., 2016).
930 From a kinetic perspective, higher surface temperatures would be expected to increase the uptake
931 rates of nutrients, including micronutrients like Fe, Co and Zn, by increasing the value of K_M.
932 However, the effects of temperature on productivity and community composition are more
933 complex since increasing ocean temperatures would also decrease the solubility of CO_2, change
934 the seasonality of ice cover and thus sunlight availability, and affect water column turnover and
935 mixing regimes (Rose et al., 2009). The effects of warming temperatures on the intricate landscape
936 of nutrient availability and limitation regimes described here is an open question in this study.

937 4.7 A two-box model that describes a mechanism for deep dCo inventory loss

938   To test the proposed mechanism that higher Co uptake rates and winter mixing can lead to
939 a deep inventory loss of ~10 pM Co over 12 years, a time step two-box model of a 1 m^2 water
940 column was created in Microsoft Excel to simulate the Ross Sea dCo cycle. A schematic of the
941 modeled dCo cycle is presented in Fig. 11, flux equations to describe the biogeochemical cycling
942 of Co are presented in Appendix C, and the parameters used to simulate dCo loss over 12 years
943 and a hypothetical steady state condition are given in Table 6.

944   The change in dCo concentration over time (d[dCo]/dt) for a surface ocean (0–100 m) and
945 deep ocean (100–500 m) was calculated as the sum of the dCo source fluxes minus the sum of the
946 sink fluxes:

947
$$\left(\frac{d[dCo]}{dt}\right)_{Surface} = \frac{F_{Over} + F_{Remin} - F_{Up}}{V_{Surface}}$$

948
$$\left(\frac{d[dCo]}{dt}\right)_{Deep} = \frac{F_{Remin} + F_{Neph} - F_{Up} - F_{Over}}{V_{Deep}}$$

949   where F_{Over} is the overturning flux between the two boxes, F_{Remin} is the remineralization flux, F_{Up}
950   is the biological uptake flux, and F_{Neph} is the flux of dCo from the nepheloid layer into the deep
951   ocean (Table C1). F_{Up} was calculated using the measured ρCo uptake rates observed on the
952   CORSACS and CICLOPS expeditions, and F_{Remin} was calculated using an assumed surface and
953   deep remineralization factor (RF) of 0.9, indicating that 90% of the POM generated in the surface
954   ocean is remineralized back to its inorganic dissolved components. In the Southern Ocean, the
955   fluxes of scavenging and aerosol deposition would be relatively negligible, so these fluxes have
956   been omitted from the model. The magnitude of F_{Neph} in the Ross Sea remains unconstrained, and
957   in this model, the deep nepheloid dCo source was used as an adjustable parameter to tune the
958   magnitude of deep dCo loss to be 10 pM over 12 years, which represents the approximate observed
959   differences between the CORSACS and CICLOPS expeditions detailed in Sect. 4.3. A F_{Neph} was
960   calculated to be 3550 pmol dCo m^{-2} d^{-1} to the deep ocean, but this should not be considered a
961   meaningful calculation of the observed nepheloid layer flux.
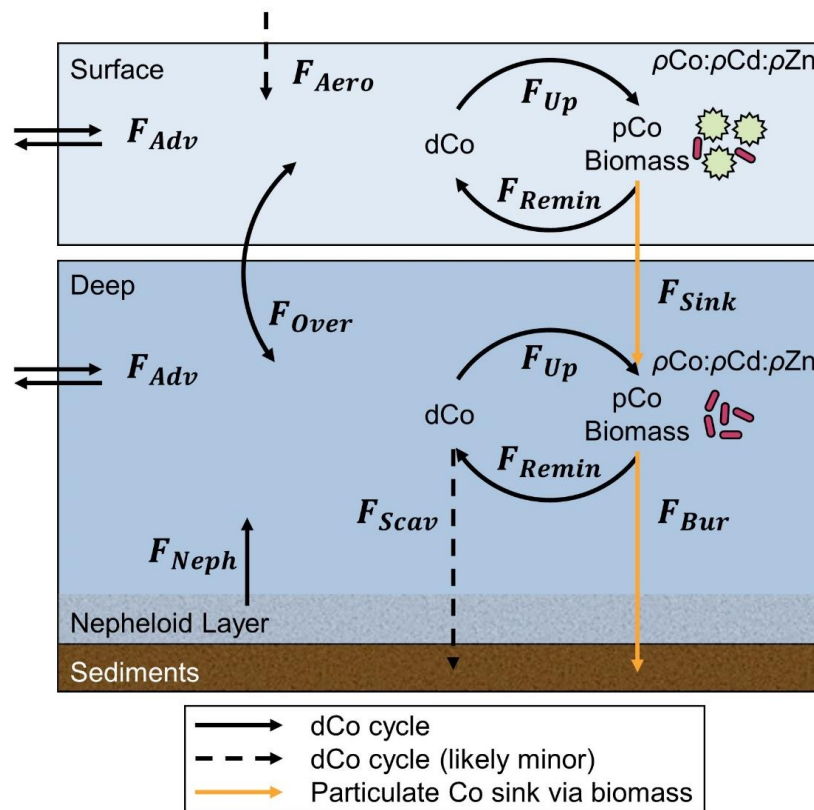
962
963   **Figure 11.** A schematic of the dCo cycle (black arrows) and select processes of the particulate Co
964   (pCo) cycle (orange arrows) presented as a simplified two-box model. Net fluxes of the dCo cycle
965   include sources from aerosol deposition (F_{Aero}), bottom sediments and the nepheloid layer (F_{Neph}),
966   and scavenging to Mn-oxides particles (F_{Scav}) which likely represents a minor flux in the coastal
967   Antarctic seas. Internal cycling fluxes include horizontal advection (F_{Adv}), water column
968   overturning or mixing (F_{Over}), biological uptake (F_{Up}) and remineralization of pCo (F_{Remin}). Fluxes
969   of pCo shown here include sinking biomass from the surface into the deep ocean (F_{Sink}) and pCo
970   burial into sediments along the seafloor (F_{Bur}). The biological uptake of dCo is influenced by the
971   relative stoichiometric uptake of Co, Zn and Cd (ρCo : ρCd : ρZn) among the microbial
972   community. Differential equations that describe and quantify these fluxes are presented in
973   Appendix C.

974   In the Ross Sea, the deep winter mixed layer can extend 600 m to the seafloor and turn
975 over the whole water column in some locations (Smith and Jones, 2015), mixing the surface and
976 deep ocean under the winter sea ice and resulting in near-vertical profiles of dCo in the early spring
977 (Noble et al., 2013). Here, the winter mixing process was modeled by combining the surface and
978 deep ocean boxes into one homogenized box during the winter season (151 days, ~5 months). The
979 dCo concentrations of the winter box were calculated using a volume-weighted average (see
980 Appendix C).

981 **Table 6.** Parameters of the Co cycle two-box model, run as both a steady state model with lower
982 Co uptake rates (ρCo) and as a mechanism for deep dCo inventory loss driven by higher ρCo
983 values. The calculated burial flux of particulate Co within each model variation is also given, but
984 note that the burial flux values should be interpreted as a comparison of the Co sink via the
985 biological pump when ρCo is varied, and not as observed or meaningful Co flux magnitudes.

Model Parameters	Value	Units
Bloom season length	214	days
Surface box height	100	m
Deep box height	500	m
Remineralization Factor (RF)	0.9	
Deep Nephloid Flux	3550	pmol Co m^{-2} d^{-1}
Overturning Water Flux	0	m^3 d^{-1}
Steady State Parameters		
Surface ρ Co	0.27	pmol Co L^{-1} d^{-1}
Deep ρ Co	0.66	pmol Co L^{-1} d^{-1}
Burial Flux	3550	pmol Co d^{-1}
Co Loss Parameters		
Surface ρ Co	0.87	pmol Co L^{-1} d^{-1}
Deep ρ Co	0.1	pmol Co L^{-1} d^{-1}
Burial Flux	5870	pmol Co d^{-1}

986

987   This model provides a plausible mechanism by which increases in ρCo such as those
988 observed along the CICLOPS expedition might increase the burial flux of particulate Co, resulting
989 in a net loss to the deep dCo inventory. The uptake rate of Co both within and below the photic
990 zone, as well as the fraction of POM that is remineralized, dictated the flux of particulate Co into
991 the sediments via burial. The initial dCo concentration was set at 56 pM, which approximates the
992 mean deep dCo concentrations observed on both CORSACS-1 and CORSACS-2. When the model
993 was run for 12 years, the time period between the first CORSACS expedition and the CICLOPS
994 expedition, it generated a sawtooth pattern; the surface and deep boxes diverged over the course
995 of the summer bloom season as biological uptake removed dCo from the surface box and
996 remineralization replenished dCo in the deep box (Fig. 12). Winter mixing then unified and reset
997 the water column, replenishing the surface dCo inventory. The model was run at a steady state
998 using the average surface ρCo rate observed on CORSACS-1 (0.27 pmol L^{-1} d^{-1}; Table 6) (Saito
999 et al., 2010) and deep ρCo values that were tuned to allow no change in the deep dCo inventory
1000 every winter. When the model was run using representative surface and deep ρCo values observed
1001 on the CICLOPS expedition (0.87 and 0.1 pmol Co L^{-1} d^{-1}, respectively), the surface depletion of

1002 dCo was more pronounced by the end of the bloom season compared to the steady state model,
1003 and winter mixing resulted in a steady annual decrease of the deep dCo inventory. The mechanism
1004 of dCo loss was driven by increasing ρCo, particularly in the surface ocean, and the propagation
1005 of dCo loss into the deep ocean via vertical mixing. The resulting burial flux when the model
1006 exhibited a deep dCo loss mechanism was higher than when the model was run at a steady state
1007 (Table 6), demonstrating how higher Co uptake rates among plankton paired with a deep winter
1008 mixed layer can result in a diminishing dCo inventory on a decadal timescale.
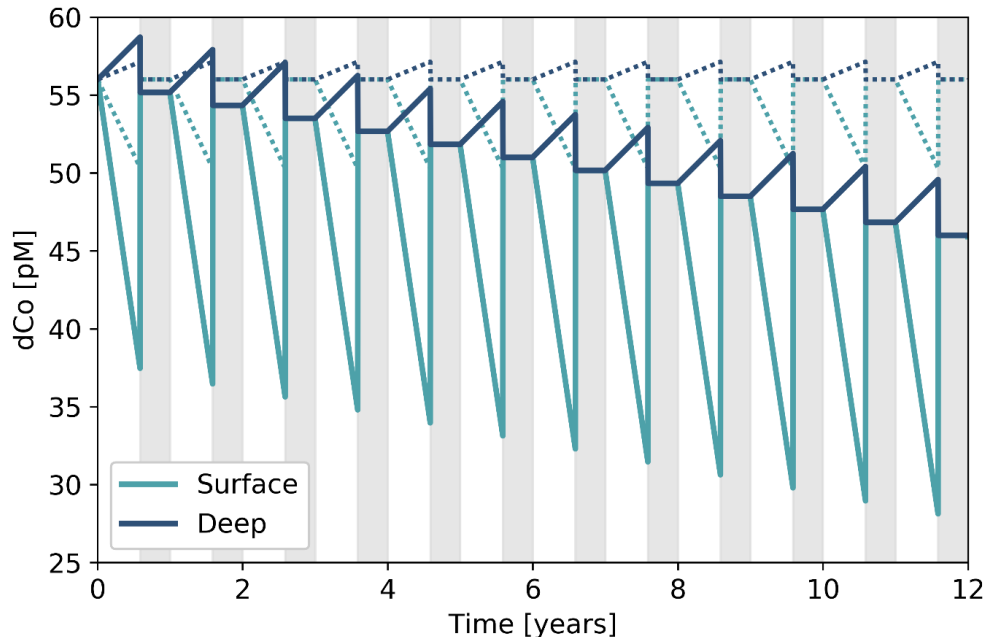
1009
1010 **Figure 12.** Results of the two-box model illustrating a potential mechanism for the loss of the dCo
1011 inventory over time. Gray boxes represent the winter season when the surface and deep boxes mix.
1012 The dotted lines represent a system at a steady state, where the dCo inventory stays consistent
1013 annually. The solid lines represent a system exhibiting dCo loss, where increased Co uptake rates
1014 in both the surface and deep ocean result in an annually decreasing dCo inventory. The initial deep
1015 dCo concentration was 56 pM, which approximates the mean deep dCo concentrations observed
1016 on CORSACS-1 and CORSACS-2. Over 12 years, the dCo loss model depicts the loss of 0.83 pM
1017 year^{-1} to end at a deep dCo inventory of 46 pM, the mean deep dCo concentration observed on
1018 CICLOPS.

1019   The purpose of this model was to illustrate a possible mechanism for a dCo inventory loss
1020 over the 12-year period between the CORSACS and CICLOPS expeditions using reasonable
1021 estimates of Co uptake and other Co cycle fluxes to achieve the observed 10 pM deep inventory
1022 loss. This box model successfully shows the directionality of the changes to the deep ocean dCo
1023 inventory and deep burial flux when the ρCo values increase, but the magnitude of the estimated
1024 Co burial or the nepheloid Co source should not be considered meaningful flux values. The model
1025 represented a greatly simplified version of the carbon pump in the Southern Ocean, and it is likely
1026 that at least some of the unquantified Co cycle fluxes were not negligible, including horizontal
1027 advection, overturning water during the summer season, Co scavenging, and a surface aerosol
1028 source. Additionally, it is a simplifying assumption that ρCo values would be consistent throughout
1029 a surface or deep depth region, as well as consistent over an entire summer season. Despite its

1030 simplicity, the box model presented a concise and reasonable mechanism for this study's
1031 observation of a shrinking dCo inventory in the Ross Sea.

5 Conclusion

1033   The Ross Sea, Amundsen Sea and Terra Nova Bay displayed lower dCo and labile dCo
1034 inventories during the 2017/2018 austral summer relative to prior observations in the region, which
1035 is consistent with observations of higher rates of Co use and uptake by phytoplankton and
1036 heterotrophic bacteria. The near-100% complexation of the dCo inventory reveals that the dCo
1037 loss is primarily due to the uptake of labile dCo, the most bioavailable form of dCo to marine
1038 microbes. The decrease in dCo throughout the water column compared to prior observations is
1039 indicative of a multi-year mechanism, whereby the removal of dCo from the surface mixed layer
1040 via uptake over the summer has been propagated into the deep ocean via winter mixing, resulting
1041 in a decrease in dCo concentration throughout the water column. This mechanism is reliant upon
1042 increased dCo uptake into organic matter and an increase in the burial rate of Co as organic matter.
1043 The observed biogeochemical differences may be due to the alleviation of Fe limitation through
1044 inputs from increased glacial melting and subsequent development of intermittent vitamin B_{12}
1045 and/or Zn limitation, both of which would be expected to increase the demand for Co among
1046 plankton communities.

1047   In coastal Antarctica and other regions impacted by global climate change, Co is a
1048 noteworthy trace metal nutrient to investigate because its small inventory and flexible
1049 phytoplankton stoichiometry make its biogeochemical cycle particularly vulnerable to
1050 perturbation. In the Arctic Ocean, for example, the dCo and labile dCo inventories have increased
1051 as melting ice and permafrost have increased the flux of Co-enriched riverine waters and sediments
1052 to the upper ocean (Bundy et al., 2020). Like many other trace nutrients, the Co cycle is integrally
1053 connected to that of other elements like Zn, Cd, Fe and carbon, and observations of perturbed Co
1054 inventories and changing nutrient limitation regimes would affect their biogeochemical cycles as
1055 well. In highly productive coastal Antarctic seas, shifts in micronutrient inventories and growth
1056 limitation could have implications for the composition of regional phytoplankton blooms and the
1057 magnitude of the Southern Ocean carbon sink.

1058   Since the late 1980s, it has been hypothesized that the primary productivity and net carbon
1059 sequestration flux of the Southern Ocean is controlled by the supply of Fe to surface waters (Martin
1060 1990; Martin et al., 1990). This theory, called the "iron hypothesis", posits that the addition of
1061 bioavailable Fe to an Fe-limited surface ocean stimulates productivity and, in turn, increases the
1062 regional and possibly global carbon sequestration flux from the atmosphere into deep ocean
1063 sediments. When applied to potential carbon dioxide removal (CDR) geoengineering projects, the
1064 iron hypothesis provides a theoretical framework for ocean iron fertilization (OIF), where
1065 significant quantities of Fe are introduced to the surface Southern Ocean to enhance the net
1066 sequestration of CO_2 and reduce global atmospheric CO_2 concentrations (Emerson, 2019). Over
1067 the past three decades, several mesoscale Fe fertilization experiments have shown that large
1068 phytoplankton blooms can be stimulated by the addition of Fe to the surface Southern Ocean, and
1069 that the impact on the CO_2 sink is variable, modest and often difficult to assess (Coale et al., 1996;
1070 Boyd et al., 2000; de Baar et al., 2005; Smetacek et al., 2012). This study provides additional
1071 insights into the potential of OIF, suggesting that the alleviation of Fe limitation might shift the
1072 region towards the limitation of another trace nutrient such as vitamin B_{12}, Zn, and potentially Co.
1073 The nutrient limitation regimes of the Southern Ocean are complex, heterogeneous and possibly

1074 shifting on decadal timescales, and these intricacies must be examined when considering future
1075 OIF projects.

1076 **Appendix A. Locations and hydrography of historical Ross Sea and Terra Nova Bay stations**
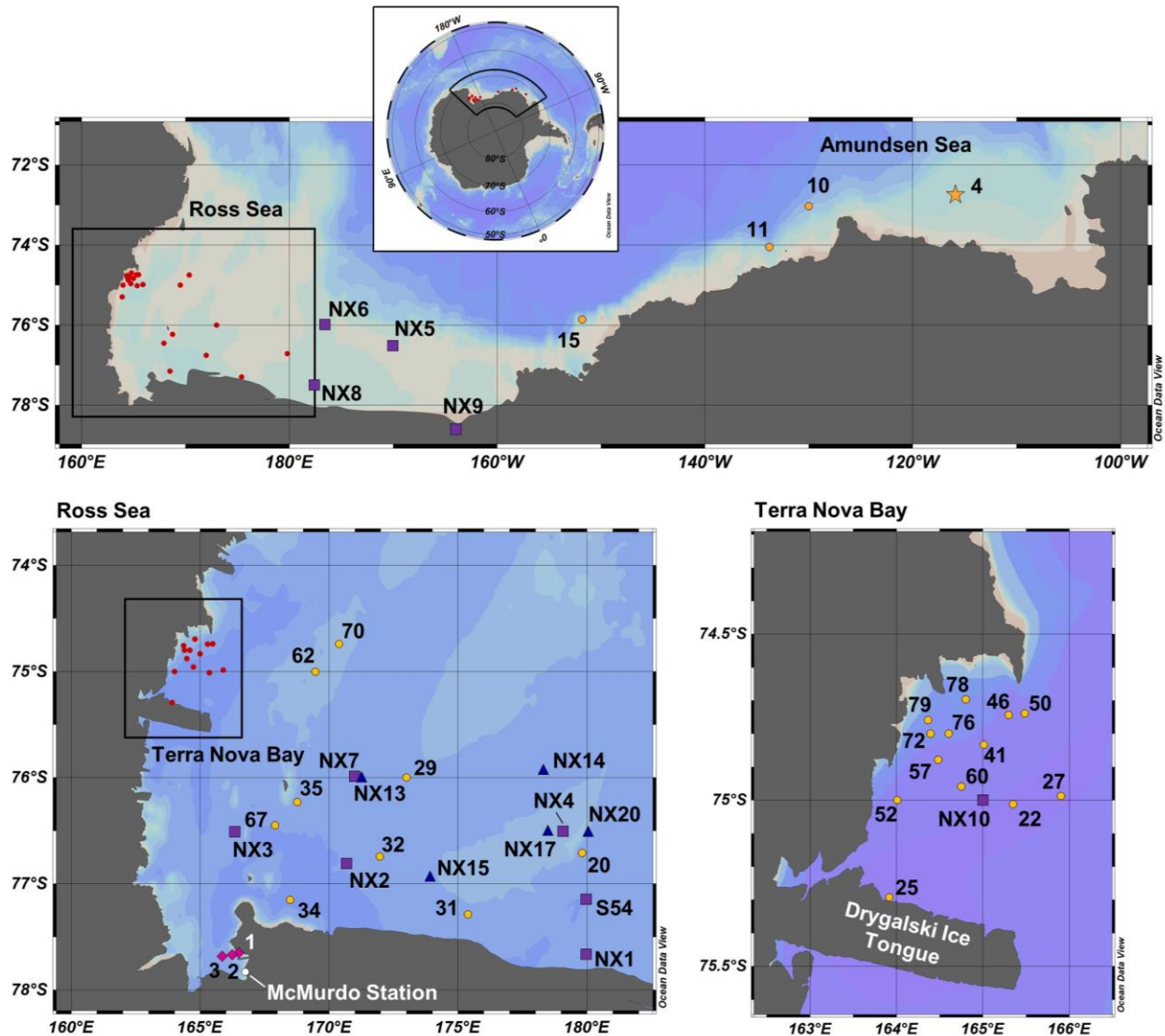
1077

1078 **Figure A1.** Map of CICLOPS (yellow circles), CORSACS-1 (purple squares), CORSACS-2 (blue
1079 triangles) and McMurdo Sounds fieldwork (magenta diamonds) stations in coastal Antarctic
1080 waters, including insets of stations within the Ross Sea and Terra Nova Bay. Only stations from
1081 the CORSACS-1 and CORSACS-2 expeditions whose data is used in this study are shown.
1082 Stations marked in red are CICLOPS stations shown in more detail in an inset. Note that the grey
1083 coastline marks both terrestrial coastline and areas of consistent ice, including ice shelves and
1084 glaciers; this includes the Drygalski Ice Tongue, a glacier to the south of Terra Nova Bay.
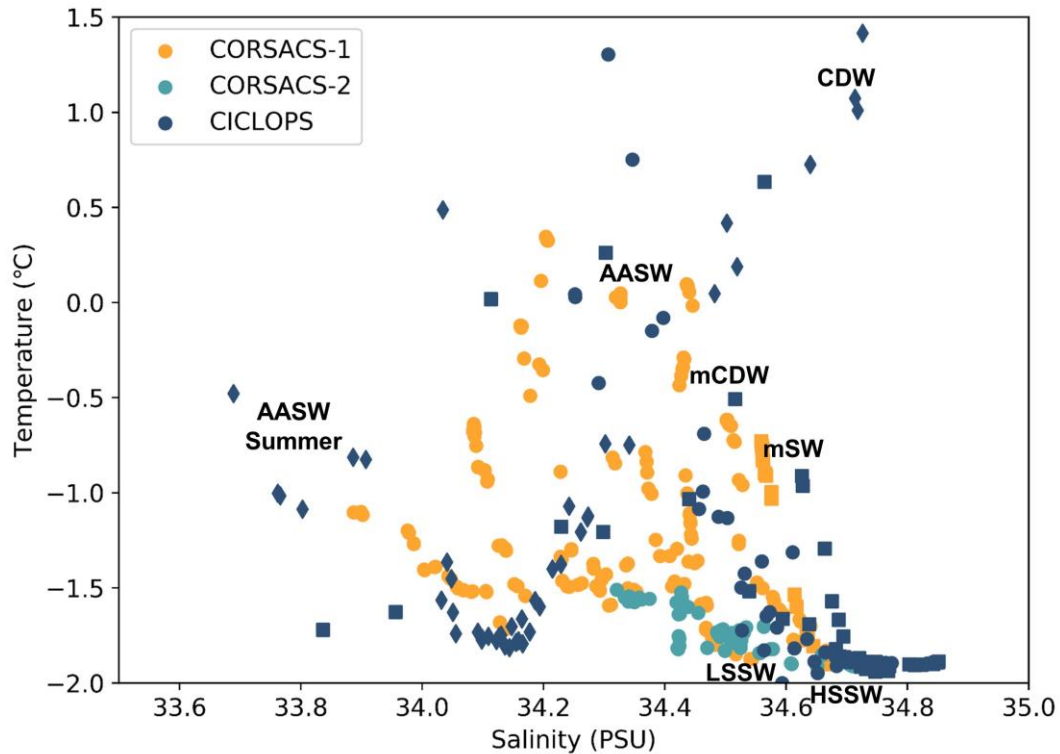
1085

Figure A2. The Temperature-Salinity relationship and water mass classification of samples from the Amundsen Sea (diamonds), Ross Sea (circles) and Terra Nova Bay (squares). Sample data is shown only from samples used to compare dCo data from the CORSACS-1, CORSACS-2 and CICLOPS expeditions in Sect. 4.3. Labeled water masses include Cirumpolar Deep Water (CDW), modified Circumpolar Deep Water (mCDW) , modified Shelf Water (mSW), Low Salinity Shelf Water (LSSW), High Salinity Shelf Water (HSSW), Antarctic Surface Water (AASW), and the fresher summertime AASW (AASW Summer). Classification of water mass samples from the CICLOPS expedition are taken from Rao (2020), Figure 3-25 and references therein. Note that the CORSACS-1, CORSACS-2 and CICLOPS expeditions largely overlapped in their water mass distribution in the Ross Sea and Terra Nova Bay.

Appendix B. Estimating trace metal uptake and maximum rate of dissolution profiles from classic competitive inhibition equations.
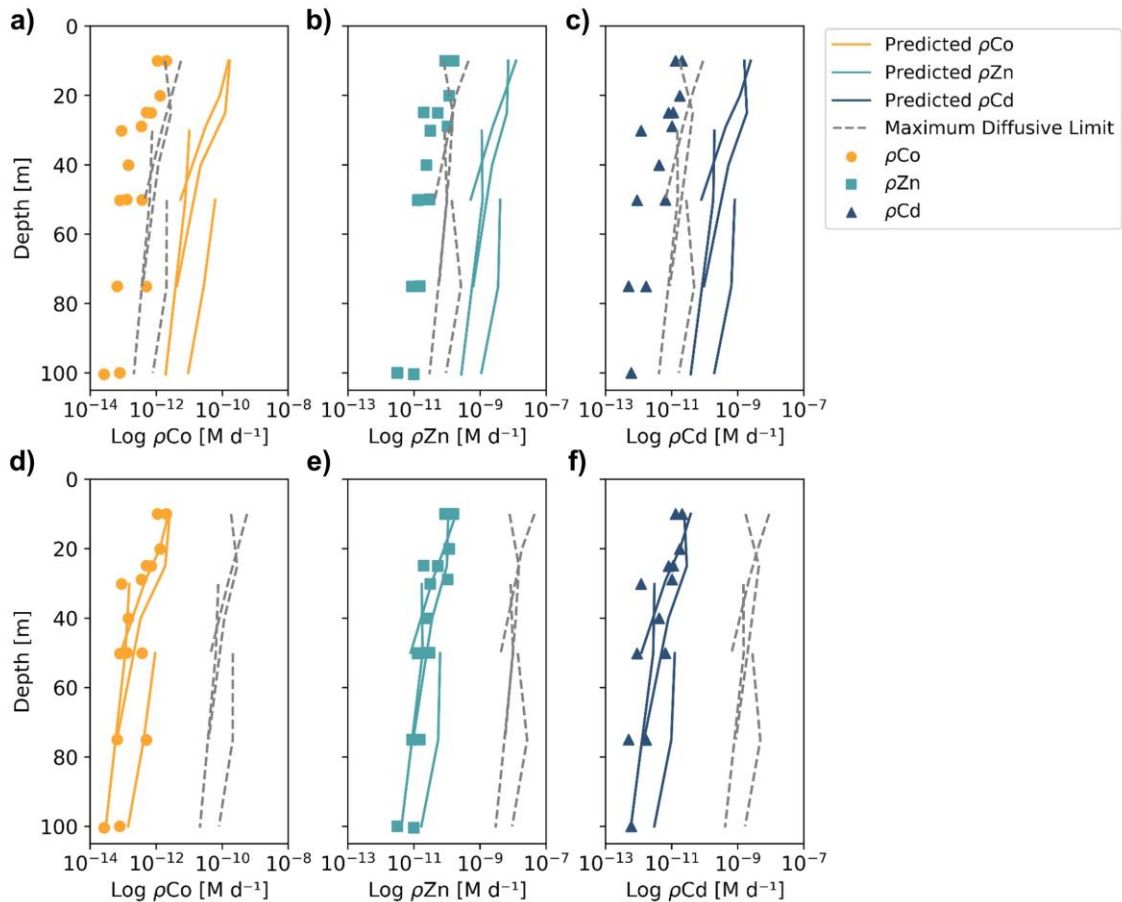
Figure B1. Observed (markers) and predicted (solid lines) trace metal uptake rate (ρM) profiles and the estimated maximum diffusive limit profiles (dashed line) for Co **(a,d)** Zn **(b,e)** and Cd **(c,f)** from Stations 11, 20, 22 and 57, using different equation parameters than those used in Fig. 10. In panels a-c, the predicted uptake rates used a literature V_{max} value of 262 µmol (mol C^{-1}) d^{-1} determined from Zn^{2+} uptake experiments in *Emiliania huxleyi* cultures (Sunda and Huntsman, 1992), resulting in predicted uptake rates that were orders of magnitude greater than the observed values. In panels d-f, the estimated maximum diffusive limit profiles assumed that 100% of the dCo, dZn and dCd inventories were labile and 0% were bound to strong organic ligands, resulting in diffusive limits that were also orders of magnitude greater than the observed values. This analysis helps to show how parameter assumptions can greatly influence the predicted uptake rates and illustrates the difficulty of assigning kinetic parameters to environmental analyses.

1112
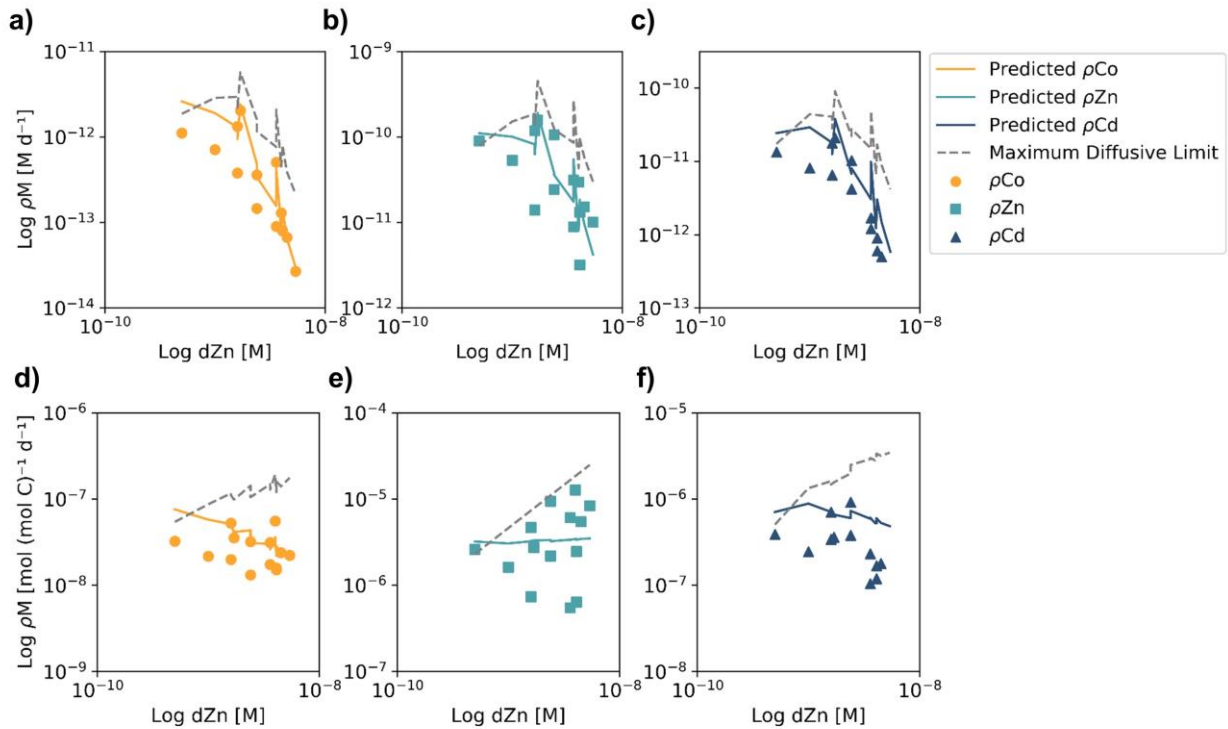
1113
1114 **Figure B2.** Observed (markers) and predicted (solid lines) trace metal uptake rates (ρM) and the
1115 estimated maximum diffusive limit profiles (dashed line) plotted against total dZn concentrations,
1116 assuming a V_{max} of 4 µmol (mol C^{-1}) d^{-1} and that 99% of the trace metal inventory was bound to
1117 strong organic ligands. Panels **a-c** show ρM in units of M d^{-1}, which tended to decrease at high
1118 dZn concentrations. This is attributable to higher dZn concentrations below the photic zone, where
1119 much lower rates of micronutrient uptake occur. Panels **d-f** show ρM when normalized to biomass
1120 using Chl-a concentrations and a C : chl-a ratio of 130 w/w (DiTullio and Smith, 1996). The
1121 normalized predicted ρZn values are relatively stable over the observed range of dZn
1122 concentrations, while the predicted ρCo and ρCd values decrease slightly as dZn increases,
1123 suggesting that competitive inhibition of ρCo and ρCd may have occurred at higher dZn
1124 concentrations due to the smaller inventories of dCo and dCd compared to dZn.
1125

Appendix C. Description of a two-box model of the dCo cycle in coastal Antarctic seas, and a potential mechanism for deep dCo loss with changing microbial uptake stoichiometry.

The two-box model described below was used to conceptualize the biogeochemical cycling of dCo in the surface and deep ocean. The model describes a 1 m^2 column of water with a total depth of 600 m and a depth threshold between the surface and deep box of 100 m. Within each box, the net change of dCo over time is equivalent to the sum of the source fluxes minus the sum of the sink fluxes:

$$\left(\frac{d[dCo]}{dt}\right)_{Surface} = \frac{\Sigma(F_i)_{Sources} - \Sigma(F_i)_{Sinks}}{V_{Surface}}$$

$$\left(\frac{d[dCo]}{dt}\right)_{Deep} = \frac{\Sigma(F_i)_{Sources} - \Sigma(F_i)_{Sinks}}{V_{Deep}}$$

where fluxes (F_i) are in units of mols dCo d^{-1}. A summary of the sources and sinks relevant to dCo in coastal Antarctic seas is shown below in Table C1. In the Southern Ocean, we would expect the fluxes of scavenging (F_{Scav}) and aerosol deposition (F_{Aero}) would be relatively negligible, and so these fluxes have been omitted from the model. Additionally, we can assume that horizontal advection is at a steady state, and thus the net advection flux is $\approx$ 0 mols dCo d^{-1}. This gives us the net equations for both boxes:

$$\left(\frac{d[dCo]}{dt}\right)_{Surface} = \frac{F_{Over} + F_{Remin} - F_{Up}}{V_{Surface}}$$

$$\left(\frac{d[dCo]}{dt}\right)_{Deep} = \frac{F_{Remin} + F_{Neph} - F_{Up} - F_{Over}}{V_{Deep}}$$

Table C1: The source and sink fluxes of dCo in the surface and deep ocean boxes. Fluxes are theoretically in units of mols dCo d^{-1}.

Surface Sources		Surface Sinks		Deep Sources		Deep Sinks	
Remineralization	F_{Remin}	Microbial Uptake	F_{Up}	Remineralization	F_{Remin}	Microbial Uptake	F_{Up}
Overturning	F_{Over}	Advection	F_{Adv}	Nepheloid Layer	F_{Neph}	Overturning	F_{Over}
Aerosols	F_{Aero}			Advection	F_{Adv}	Scavenging	F_{Scav}
Advection	F_{Adv}					Advection	F_{Adv}

Uptake fluxes

The flux of dCo incorporation into microbial biomass via uptake by protein transporters can be described using the uptake rates (ρCo) measured by ^{57}Co incubation experiments, where units of ρCo are in mols dCo L^{-1} d^{-1}:

$$F_{Up,Surface} = (\rho Co_{Surface} * V_{Surface})$$

$$F_{Up,Deep} = (\rho Co_{Deep} * V_{Deep})$$

Remineralization fluxes

In this model, the remineralization flux of particulate Co in organic matter to dCo is quantified by a Remineralization Factor (RF), which can be applied to the amount of particulate matter present in each box. Typical RF values tend to be between 0.90 and 0.99 (Glover et al., 2011), meaning that between 90% and 99% of all microbial biomass produced tends to be remineralized before sinking out of its respective box. It is not clear that the RFs for the surface and deep box should be represented by the same value, and so we have defined both surface ($RF_{Surface}$) and deep (RF_{deep}) variables here. In the surface ocean, excess Co in un-remineralized biomass will sink into the deep box (F_{Sink}), where it is further able to be remineralized in the deep ocean. In the deep ocean, excess Co in un-remineralized biomass is assumed to flux into the sediments via burial (F_{Bur}), representing a key sink of dCo biomass out of the two-box system. The surface box remineralization flux is represented with a relatively simple equation:

$$F_{Remin,Surface} = RF_{Surface} * F_{Up,Surface}$$

$$F_{Remin,Surface} = RF_{Surface}(\rho Co_{Surface} * V_{Surface})$$

The deep ocean remineralization flux can then be calculated as the sum of the remineralization flux from excess biomass that sinks as particulate Co and biomass generated in the deep ocean:

$$F_{Remin,Deep} = RF_{Deep}\left(F_{Up, Surface} - F_{Remin,Surface}\right) + RF_{Deep}(F_{Up, Deep})$$

$$F_{Remin,Deep} = RF_{Deep}(\rho Co_{Surface} * V_{Surface} - RF_{Surface}(\rho Co_{Surface} * V_{Surface})) \\ + RF_{Deep}(\rho Co_{Deep} * V_{Deep})$$

Overturning fluxes

An overturning dCo flux represents the flux of a volume of water from the deep ocean box into the shallow ocean box, and a corresponding flux of the same volume from the shallow ocean box into the deep ocean box for mass conservation. In a dynamic coastal upwelling system like the Ross and Amundsen Seas, the reality of this overturning flux is almost certainly much more complicated, as coastal upwelling processes overlap with meltwater processes and deep water mass formation processes. For the purposes of this two-box model, the flux of dCo via overturning can be estimated as a function of the overturning water flux (F_{Water}) and the dCo concentrations of each box:

$$F_{Over,Surface} = (F_{Water}[dCo]_{Deep} - F_{Water}[dCo]_{Surface})$$

$$F_{Over,Deep} = (F_{Water}[dCo]_{Surface} - F_{Water}[dCo]_{Deep})$$

In the model presented in Sect. 4.7, the F_{Water} and both F_{Over} fluxes are assumed to be negligible for the sake of modeling simplicity, but the introduction of a nonzero overturning flux would help to make the seasonal change in the dCo inventory in both the surface and deep oceans nonlinear, as it is currently the only flux in this model that is calculated using the time step's dCo concentrations.

Flux from the nepheloid layer

At several CICLOPS stations, a distinct nepheloid layer was detected as dCo concentration increased sharply at depths immediately above (~10 m) the ocean floor. The nepheloid layer tends

1194 to contain high levels of particles moving horizontally along the seafloor, and is likely a significant
1195 source of dCo to the surrounding water column. The source of dCo from the nepheloid layer is
1196 somewhat unclear; it could be via dissolution of particles suspended within the nepheloid layer or
1197 from a porewater flux of dCo out of the sediments. In this model, the flux of deep dCo inputs into
1198 the deep ocean, assumed to be from the nepheloid layer, was derived using the Microsoft Excel
1199 solver tool, given the parameter that 10 pM of deep dCo was lost over 12 years. The deep source
1200 of dCo was calculated to be 3550 pmol dCo m^{-2} d^{-1}. This value should be considered an adjustable
1201 parameter used to tune the model to our conceptual understanding of dCo inventory loss, and not
1202 a meaningful calculation of observed Co flux from the deep nepheloid layer, which has yet to be
1203 constrained.

1204 The cobalt burial sink

1205 The loss of cobalt from the deep ocean box into the sediments via burial can be quantified
1206 with the equation:

$$1207 \quad \left(\frac{d[Co]}{dt}\right)_{Bur} = F_{Sink} + F_{Up,Deep} - F_{Remin,Deep}$$

1208 where F_{Sink} is described by:

$$1209 \quad F_{Sink} = (\rho Co_{Surface} * V_{Surface}) - RF_{Surface}(\rho Co_{Surface} * V_{Surface})$$

1210 This estimate of the loss of dCo due to burial assumes that all biogenic particulate Co that is not
1211 remineralized in the surface ocean sinks into the deep ocean, and all biogenic particulate Co that
1212 is not remineralized in the deep ocean is sequestered in sediments and "lost" to the model.

1213 Modeling seasonality: the winter mixed layer

1214 In the Ross and Amundsen Seas, sea ice covers the surface ocean for a larger portion of the
1215 year (~ 5 months). During this time, the water column mixes – a process that was modeled by
1216 combining the two-box model into one homogenized box after the 7-month bloom season to
1217 simulate the winter season. This process can be modeled by a volume-weighted average with the
1218 volume of each box.

$$1219 \quad [dCo]_{Winter} = \frac{(V_{Surface} * [dCo]_{Surface}) + (V_{Deep} * [dCo]_{Deep})}{(V_{Surface} + V_{Deep})}$$

1220 **Data availability**

1221 The CICLOPS dCo dataset has been submitted to the Biological and Chemical Oceanography Data
1222 Management Office (BCO-DMO) website (https://www.bco-dmo.org/project/774945) and is
1223 pending approval for publication. The dissolved metals (dZn, dCd) dataset (https://www.bco-
1224 dmo.org/dataset/877466), Zn and Cd uptake rate dataset (https://www.bco-
1225 dmo.org/dataset/877681), and macronutrient dataset (https://www.bco-dmo.org/dataset/874841)
1226 are publicly available on the BCO-DMO website.

1227 **Author contribution**

1228 RC collected and analyzed dCo samples and wrote the manuscript. RK collected and analyzed
1229 dZn and dCd samples and measured Zn and Cd uptake rates. DR measured Co uptake rates. GD

1230 collected and analyzed phytoplankton pigment samples. All authors assisted in the collection and
1231 processing of dissolved seawater samples and incubation experiment samples, and all authors
1232 helped write the manuscript.

Competing interests

1234 The authors declare that they have no conflict of interest.

Acknowledgments

1236 The authors thank the captain, crew and science party of the RVIB *Nathaniel B. Palmer* for their
1237 support during the CICLOPS expedition. We also thank Joe Jennings (OSU) for dissolved
1238 macronutrient analysis, Véronique Oldham for sampling assistance, and Matthew Charette,
1239 Stephanie Dutkiewicz, and Alessandro Tagliabue for writing insights. This work was funded by
1240 grants from the National Science Foundation's Office of Polar Programs (OPP-1643684, OPP-
1241 1644073 and OPP-1643845).

References

1243 Arrigo, K. R., Robinson, D. H., Worthen, D. L., Dunbar, R. B., DiTullio, G. R., Vanwoert, M.
1244 and Lizotte, M. P.: Phytoplankton community structure and the drawdown of nutrients and CO2
1245 in the Southern Ocean, Science., 283, 365–367, 1999.

1246 Arrigo, K. R., van Dijken, G. L. and Bushinsky, S.: Primary production in the Southern Ocean,
1247 1997-2006, J. Geophys. Res., 113, C08004, doi:10.1029/2007JC004551, 2008.

1248 Arrigo, K. R., Lowry, K. E. and van Dijken, G. L.: Annual changes in sea ice and phytoplankton
1249 in polynyas of the Amundsen Sea, Antarctica, Deep. Res. Part II Top. Stud. Oceanogr., 71–76,
1250 5–15, doi:10.1016/j.dsr2.2012.03.006, 2012.

1251 de Baar, H. J. W., Boyd, P. W., Coale, K. H., Landry, M. R., Tsuda, A., Assmy, P., Bakker, D.
1252 C. E., Bozec, Y., Barber, R. T., Brzezinski, M. A., Buesseler, K. O., Boyé, M., Croot, P. L.,
1253 Gervais, F., Gorbunov, M. Y., Harrison, P. J., Hiscock, W. T., Laan, P., Lancelot, C., Law, C. S.,
1254 Levasseur, M., Marchetti, A., Millero, F. J., Nishioka, J., Nojiri, Y., van Oijen, T., Riebesell, U.,
1255 Rijkenberg, M. J. A., Saito, H., Takeda, S., Timmermans, K. R., Veldhuis, M. J. W., Waite, A.
1256 M. and Wong, C. S.: Synthesis of iron fertilization experiments: From the iron age in the age of
1257 enlightenment, J. Geophys. Res. C Ocean., 110(9), 1–24, doi:10.1029/2004JC002601, 2005.

1258 Bernhardt, H. and Wilhelms, A.: The continuous determination of low level iron, soluble
1259 phosphate and total phosphate with the AutoAnalyzer(TM), in Technicon Symposium, vol. 1, p.
1260 386., 1967.

1261 Bertrand, E. M., Saito, M. A., Rose, J. M., Riesselman, C. R., Lohan, M. C., Noble, A. E., Lee,
1262 P. A. and DiTullio, G. R.: Vitamin B12 and iron colimitation of phytoplankton growth in the
1263 Ross Sea, Limnol. Oceanogr., 52(3), 1079–1093, doi:10.4319/lo.2007.52.3.1079, 2007.

1264 Bertrand, E. M., Saito, M. A., Lee, P. A., Dunbar, R. B., Sedwick, P. N. and DiTullio, G. R.: Iron
1265 limitation of a springtime bacterial and phytoplankton community in the Ross Sea: implications
1266 for vitamin B12 nutrition, Front. Microbiol., 2, 160, doi:10.3389/fmicb.2011.00160, 2011.

1267 Bertrand, E. M., Moran, D. M., McIlvin, M. R., Hoffman, J. M., Allen, A. E. and Saito, M. A.:
1268 Methionine synthase interreplacement in diatom cultures and communities: Implications for the

persistence of B12 use by eukaryotic phytoplankton, Limnol. Oceanogr., 58(4), 1431–1450, doi:10.4319/lo.2013.58.4.1431, 2013.

Bown, J., Boye, M. and Nelson, D. M.: New insights on the role of organic speciation in the biogeochemical cycle of dissolved cobalt in the southeastern Atlantic and the Southern Ocean, Biogeosciences, 9, 2719–2736, doi:10.5194/bg-9-2719-2012, 2012.

Boyd, P. W., Watson, A. J., Law, C. S., Abraham, E. R., Trull, T., Murdoch, R., Bakker, D. C. E., Bowie, A. R., Buesseler, K. O., Chang, H., Charette, M., Croot, P., Downing, K., Frew, R., Gall, M., Hadfield, M., Hall, J., Harvey, M., Jameson, G., LaRoche, J., Liddicoat, M., Ling, R., Maldonado, M. T., McKay, R. M., Nodder, S., Pickmere, S., Pridmore, R., Rintoul, S., Safi, K., Sutton, P., Strzepek, R., Tanneberger, K., Turner, S., Waite, A. and Zeldis, J.: A mesoscale phytoplankton bloom in the polar Southern Ocean stimulated by iron fertilization, Nature, 407(6805), 695–702, doi:10.1038/35037500, 2000.

Brisbin, M. M., Mitarai, S., Saito, M. A. and Alexander, H.: Microbiomes of bloom-forming Phaeocystis algae are stable and consistently recruited, with both symbiotic and opportunistic modes, ISME J, doi:10.1038/s41396-022-01263-2, 2022.

Budillon, G., Salusti, E. and Tucci, S.: The evolution of density currents and nepheloid bottom layers in the Ross Sea (Antarctica), J. Mar. Res., 64(4), 517–540, doi:10.1357/002224006778715739, 2006.

Bundy, R. M., Tagliabue, A., Hawco, N. J., Morton, P. L., Twining, B. S., Hatta, M., Noble, A., Cape, M. R., John, S. G., Cullen, J. T. and Saito, M. A.: Elevated sources of cobalt in the Arctic Ocean, Biogeosciences, 17, 4745–4767, doi:https://doi.org/10.5194/bg-2020-84, 2020.

Caron, D. A., Dennett, M. R., Lonsdale, D. J., Moran, D. M. and Shalapyonok, L.: Microzooplankton herbivory in the Ross Sea, Antarctica, Deep Sea Res. II, 47, 3249–3272, 2000.

Chandler, J. W., Lin, Y., Gainer, P. J., Post, A. F., Johnson, Z. I. and Zinser, E. R.: Variable but persistent coexistence of Prochlorococcus ecotypes along temperature gradients in the ocean's surface mixed layer, Environ. Microbiol. Rep., 8(2), 272–284, doi:10.1111/1758-2229.12378, 2016.

Chappell, P. D., Vedmati, J., Selph, K. E., Cyr, H. A., Jenkins, B. D., Landry, M. R. and Moffett, J. W.: Preferential depletion of zinc within Costa Rica upwelling dome creates conditions for zinc co-limitation of primary production, J. Plankton Res., 38(2), 244–255, doi:10.1093/plankt/fbw018, 2016.

Chmiel, R., Lanning, N., Laubach, A., Lee, J.-M., Fitzsimmons, J., Hatta, M., Jenkins, W. J., Lam, P. J., Mcilvin, M., Tagliabue, A. and Saito, M. A.: Major processes of the dissolved cobalt cycle in the North and equatorial Pacific Ocean, Biogeosciences, 19, 2365–2395 [online] Available from: https://doi.org/10.5194/bg-19-2365-2022, 2022.

Church, M. J., Hutchins, D. A. and Ducklow, H. W.: Limitation of bacterial growth by dissolved organic matter and iron in the Southern Ocean, Appl. Environ. Microbiol., 66(2), 455–466, doi:10.1128/AEM.66.2.455-466.2000, 2000.

Coale, K. H., Johnson, K. S., Fitzwater, S. E., Gordon, R. M., Tanner, S., Chavez, F. P., Ferioli, L., Sakamoto, C., Rogers, P., Millero, F., Steinberg, Pa., Nightingale, P., Cooper, D., Cochlan, W. P., Landry, M. R., Constantinou, J., Rollwagen, G., Trasvina, A. and Kudela, R.: A massive

phytoplankton bloom induced by an ecosystem-scale iron fertilization experiment in the equatorial Pacific Ocean, Nature, 383(334), 495–501, 1996.

Cohen, N. R., McIlvin, M. R., Moran, D. M., Held, N. A., Saunders, J. K., Hawco, N. J., Brosnahan, M., DiTullio, G. R., Lamborg, C., McCrow, J. P., Dupont, C. L., Allen, A. E. and Saito, M. A.: Dinoflagellates alter their carbon and nutrient metabolic strategies across environmental gradients in the central Pacific Ocean, Nat. Microbiol., 6, 173–186, doi:10.1038/s41564-020-00814-7, 2021.

Croft, M. T., Lawrence, A. D., Raux-deery, E., Warren, M. J. and Smith, A. G.: Algae acquire vitamin B12 through a symbiotic relationship with bacteria, Nature, 438, 90–93, doi:10.1038/nature04056, 2005.

DiTullio, G. and Geesey, M. E.: Photosynthetic Pigments in Marine Algae and Bacteria, in Encyclopedia of Environmental Microbiology, edited by G. Bitton, pp. 2453–2470, John Wiley & Sons, Inc., New York, NY., 2003.

DiTullio, G. R., Grebmeier, J. M., Arrigo, K. R. and Lizotte, M. P.: Rapid and early export of Phaeocystis antarctica blooms in the Ross Sea , Antarctica, Nature, 404, 595–598, 2000.

DiTullio, G. R. and Smith, W. O. J.: Spatial patterns in phytoplankton biomass and pigment distributions in the Ross Sea, J. Geophys. Res., 101, 18467–18477, 1996.

DiTullio, G. R., Geesey, M. E., Jones, D. R., Daly, K. L., Campbell, L. and Smith, W. O. J.: Phytoplankton assemblage structure and primary productivity along 170° W in the South Pacific Ocean, Mar. Ecol. Prog. Ser., 255, 55–80, 2003.

DiTullio, G. R., Garcia, N., Riseman, S. F. and Sedwick, P. N.: Effects of iron concentration on pigment composition in *Phaeocystis antarctica* grown at low irradiance, Biogeochemistry, 83, 71–81, doi:10.1007/s10533-007-9080-8, 2007.

Ducklow, H., Carlson, C., Church, M., Kirchman, D., Smith, D. and Steward, G.: The seasonal development of the bacterioplankton bloom in the Ross Sea, Antarctica, 1994-1997, Deep. Res. Part II, 48, 4199–4221, 2001.

Ellwood, M. J., Van Den Berg, C. M. G., Boye, M., Veldhuis, M., de Jong, J. T. M., de Baar, H. J. W., Croot, P. L. and Kattner, G.: Organic complexation of cobalt across the Antarctic Polar Front in the Southern Ocean, Mar. Freshw. Res., 56, 1069–1075, doi:10.1071/MF05097, 2005.

Emerson, D.: Biogenic iron dust: A novel approach to ocean iron fertilization as a means of large scale removal of carbon dioxide from the atmosphere, Front. Mar. Sci., 6, 22, doi:10.3389/fmars.2019.00022, 2019.

Fitzwater, S. E., Johnson, K. S., Gordon, R. M., Coale, K. H. and Smith, W. O.: Trace metal concentrations in the Ross Sea and their relationship with nutrients and phytoplankton growth, Deep. Res. Part II, 47, 3159–3179, 2000.

Gardner, W. D., Richardson, M. J. and Mishonov, A. V.: Global assessment of benthic nepheloid layers and linkage with upper ocean dynamics, Earth Planet. Sci. Lett., 482, 126–134, doi:10.1016/j.epsl.2017.11.008, 2018.

Glover, D., Jenkins, W. and Doney, S.: Modeling Methods for Marine Science, Cambridge University Press, New York., 2011.

Hawco, N. J., Ohnemus, D. C., Resing, J. A., Twining, B. S. and Saito, M. A.: A dissolved cobalt plume in the oxygen minimum zone of the eastern tropical South Pacific, Biogeosciences, 13(20), 5697–5717, doi:10.5194/bg-13-5697-2016, 2016.

Hawco, N. J., Lam, P. J., Lee, J., Ohnemus, D. C., Noble, A. E., Wyatt, N. J., Lohan, M. C. and Saito, M. A.: Cobalt scavenging in the mesopelagic ocean and its influence on global mass balance: Synthesizing water column and sedimentary fluxes, Mar. Chem., (August), doi:10.1016/j.marchem.2017.09.001, 2017.

Helliwell, K. E.: The roles of B vitamins in phytoplankton nutrition: new perspectives and prospects, New Phytol., 216, 62–68, doi:10.1111/nph.14669, 2017.

Irving, H. and Williams, R. J. P.: Order of stability of metal complexes, Nature, 162, 746–747, 1948.

Jakuba, R. W., Moffett, J. W. and Dyhrman, S. T.: Evidence for the linked biogeochemical cycling of zinc, cobalt, and phosphorus in the western North Atltic Ocean, Global Biogeochem. Cycles, 22(4), GB4012, doi:10.1029/2007GB003119, 2008.

Jakuba, R. W., Saito, M. A., Moffett, J. W. and Xu, Y.: Dissolved zinc in the subarctic North Pacific and Bering Sea: Its distribution, speciation, and importance to primary producers, Global Biogeochem. Cycles, 26, GB2015, doi:10.1029/2010GB004004, 2012.

John, S. G., Geis, R. W., Saito, M. A. and Boyle, E. A.: Zinc isotope fractionation during high-affinity and low-affinity zinc transport by the marine diatom Thalassiosira oceanica, Limnol. Oceanogr., 52(6), 2710–2714, doi:10.4319/lo.2007.52.6.2710, 2007.

Kellogg, R. M.: Assessing the potential for Zn limitation of marine primary production: proteomic characterization of the low Zn stress response in marine diatoms, Massachusetts Institute of Technology; the Woods Hole Oceanographic Institution., 2022.

Kellogg, R. M., McIlvin, M. R., Vedamati, J., Twining, B. S., Moffett, J. W., Marchetti, A., Moran, D. M. and Saito, M. A.: Efficient zinc/cobalt interreplacement in northeast Pacific diatoms and relationship to high surface dissolved Co : Zn ratios, Limnol. Oceanogr., 65(11), 2557–2582, doi:10.1002/lno.11471, 2020.

Kellogg, R. M., Moosburner, M. A., Cohen, N. R., Hawco, N. J., McIlvin, M. R., Moran, D. M., DiTullio, G. R., Subhas, A. V., Allen, A. E. and Saito, M. A.: Adaptive responses of marine diatoms to zinc scarcity and ecological implications, Nat. Commun., 13, doi:10.1038/s41467-022-29603-y, 2022.

Kellogg, R. M., Schanke, N. L., Lees, L. E., Chmiel, R. J., Rao, D., Brisbin, M. M., Moran, D. M., McIlvin, M. R., Bolinesi, F., Casotti, R., Balestra, C., Horner, T. J., Subhas, A. V., Dunbar, R. B., Allen, A. E., DiTullio, G. R. and Saito, M. A.: Zinc co-limitation of natural marine phytoplankton assemblages in coastal Antarctica [Submitted].

Lane, T. W., Saito, M. A., George, G. N., Pickering, I. J., Prince, R. C. and Morel, F. M. M.: A cadmium enzyme from a marine diatom, Nature, 435, 42–42, doi:https://doi.org/10.1038/435042a, 2005.

Lee, J. G. and Morel, F. M. M.: Replacement of zinc by cadmium in marine phytoplankton, Mar. Ecol. Prog. Ser., 127, 305–309, doi:10.3354/meps127305, 1995.

Marsay, C. M., Sedwick, P. N., Dinniman, M. S., Barrett, P. M., Mack, S. L. and McGillicuddy, D. J.: Estimating the benthic efflux of dissolved iron on the Ross Sea continental shelf, Geophys. Res. Lett., 41(21), 7576–7583, doi:10.1002/2014GL061684, 2014.

Martin, J. H.: Glacial-interglacial CO2 change: the iron hypothesis, Paleoceanography, 5(1), 1–13, doi:https://doi.org/10.1029/PA005i001p00001, 1990.

Martin, J. H., Fitzwater, S. E. and Gordon, R. M.: Iron deficiency limits phytoplankton growth in Antarctic waters, Global Biogeochem. Cycles, 4(1), 5–12, 1990.

Mazzotta, M. G., McIlvin, M. R., Moran, D. M., Wang, D. T., Bidle, K. D., Lamborg, C. H. and Saito, M. A.: Characterization of the metalloproteome of Pseudoalteromonas (BB2-AT2): biogeochemical underpinnings for zinc, manganese, cobalt, and nickel cycling in a ubiquitous marine heterotroph, Metallomics, 13, mfab060, doi:https://doi.org/10.1093/mtomcs/mfab060, 2021.

Monien, D., Monien, P., Brünjes, R., Widmer, T., Kappenberg, A., Silva Busso, A. A., Schnetger, B. and Brumsack, H.-J.: Meltwater as a source of potentially bioavailable iron to Antarctica waters, Antarct. Sci., 29(03), 277–291, doi:10.1017/S095410201600064X, 2017.

Morel, F. M. M., Reinfelder, J. R., Roberts, S. B., Chamberlain, C. P., Lee, J. G. and Yee, D.: Zinc and carbon co-limitation of marine phytoplankton, Nature, 369(6483), 740–742, doi:10.1038/369740a0, 1994.

Morel, F. M. M., Lam, P. J. and Saito, M. A.: Trace Metal Substitution in Marine Phytoplankton, Annu. Rev. Earth Planet. Sci., 48, 491–517, doi:10.1146/annurev-earth-053018-060108, 2020.

Noble, A. E., Saito, M. A., Maiti, K. and Benitez-Nelson, C. R.: Cobalt, manganese, and iron near the Hawaiian Islands: A potential concentrating mechanism for cobalt within a cyclonic eddy and implications for the hybrid-type trace metals, Deep. Res. Part II Top. Stud. Oceanogr., 55(10–13), 1473–1490, doi:10.1016/j.dsr2.2008.02.010, 2008.

Noble, A. E., Moran, D. M., Allen, A. E. and Saito, M. A.: Dissolved and particulate trace metal micronutrients under the McMurdo Sound seasonal sea ice: basal sea ice communities as a capacitor for iron, Front. Chem., 1, 25, doi:10.3389/fchem.2013.00025, 2013.

Noble, A. E., Ohnemus, D. C., Hawco, N. J., Lam, P. J. and Saito, M. A.: Coastal sources, sinks and strong organic complexation of dissolved cobalt within the US North Atlantic GEOTRACES transect GA03, Biogeosciences, 14(11), 2715–2739, doi:10.5194/bg-14-2715-2017, 2017.

Oldham, V. E., Chmiel, R., Hansel, C. M., DiTullio, G. R., Rao, D. and Saito, M.: Inhibited manganese oxide formation hinders cobalt scavenging in the Ross Sea, Global Biogeochem. Cycles, 35, e2020GB006706, doi:10.1029/2020GB006706, 2021.

Osman, D., Cooke, A., Young, T. R., Deery, E., Robinson, N. J. and Warren, M. J.: The requirement for cobalt in vitamin B12: A paradigm for protein metalation, Biochim. Biophys. Acta - Mol. Cell Res., 1868, 118896, doi:10.1016/j.bbamcr.2020.118896, 2021.

Peloquin, J. A. and Smith, W. O. J.: Phytoplankton blooms in the Ross Sea, Antarctica: Interannual variability in magnitude, temporal patterns, and composition, J. Geophys. Res., 112, C08013, doi:10.1029/2006JC003816, 2007.

Planquette, H., Sherrell, R. M., Stammerjohn, S. and Field, M. P.: Particulate iron delivery to the water column of the Amundsen Sea, Antarctica, Mar. Chem., 153, 15–30, doi:10.1016/j.marchem.2013.04.006, 2013.

Price, N. M., Harrison, G. I., Hering, J. G., Hudson, R. J., Pascale, M., Nirel, V., Palenik, B. and Morel, F. M. M.: Preparation and Chemistry of the Artificial Algal Culture Medium Aquil, Biol. Oceanogr., 6, 443–461, 2013.

Rao, D.: Characterizing cobalamin cycling by Antarctic marine microbes across multiple scales, Massachusetts Institute of Technology; the Woods Hole Oceanographic Institution., 2020.

Rao, D., Fussy, Z., Moran, D. M., McIlvin, M. R., Allen, A. E., Follows, M. J. and Saito, M. A.: Flexible B12 ecophysiology of Phaeocystis antarctica to a fusion B12-independent methionine synthase with widespread homologues [In review]., PNAS [online] Available from: http://arxiv.org/abs/1712.09707.

Roberts, S. B., Lane, T. W. and Morel, F. M. M.: Carbonic Anhydrase in the Marine Diatom Thalassiosira Weissflogii (Bacillariophyceae), J. Phycol., 33(5), 845–850, doi:10.1111/j.0022-3646.1997.00845.x, 1997.

Rodionov, D. A., Vitreschak, A. G., Mironov, A. A. and Gelfand, M. S.: Comparative genomics of the vitamin B12 metabolism and regulation in prokaryotes, J. Biol. Chem., 278(42), 41148–41159, doi:10.1074/jbc.M305837200, 2003.

Rose, J. M., Feng, Y., DiTullio, G. R., Dunbar, R. B., Hare, C. E., Lee, P. A., Lohan, M., Long, M., Smith, W. O., Sohst, B., Tozzi, S., Zhang, Y. and Hutchins, D. A.: Synergistic effects of iron and temperature on Antarctic phytoplankton and microzooplankton assemblages, Biogeosciences, 6, 3131–3147, doi:10.5194/bg-6-3131-2009, 2009.

Saito, M. A. and Goepfert, T. J.: Zinc-cobalt colimitation of Phaeocystis antarctica, Limnol. Oceanogr., 53(1), 266–275, 2008.

Saito, M. A. and Moffett, J. W.: Complexation of cobalt by natural organic ligands in the Sargasso Sea as determined by a new high-sensitivity electrochemical cobalt speciation method suitable for open ocean work, Mar. Chem., 75(1–2), 49–68, doi:10.1016/S0304-4203(01)00025-1, 2001.

Saito, M. A., Rocap, G. and Moffett, J. W.: Production of cobalt binding ligands in a Synechococcus feature at the Costa Rica upwelling dome, Limnol. Oceanogr., 50(1), 279–290, 2005.

Saito, M. A., Goepfert, T. J., Noble, A. E., Bertrand, E. M., Sedwick, P. N. and DiTullio, G. R.: A seasonal study of dissolved cobalt in the Ross Sea, Antarctica: micronutrient behavior, absence of scavenging, and relationships with Zn, Cd, and P, Biogeosciences, 7, 4059–4082, doi:10.5194/bg-7-4059-2010, 2010.

Saito, M. A., Noble, A. E., Hawco, N., Twining, B. S., Ohnemus, D. C., John, S. G., Lam, P., Conway, T. M., Johnson, R., Moran, D. and McIlvin, M.: The acceleration of dissolved cobalt's ecological stoichiometry due to biological uptake, remineralization, and scavenging in the Atlantic Ocean, Biogeosciences, 14(20), 4637–4662, doi:10.5194/bg-14-4637-2017, 2017.

1469 Sañudo-Wilhelmy, S. A., Gobler, C. J., Okbamichael, M. and Taylor, G. T.: Regulation of
1470 phytoplankton dynamics by vitamin B12, Geophys. Res. Lett., 33(4), 10–13,
1471 doi:10.1029/2005GL025046, 2006.

1472 Sedwick, P. N. and DiTullio, G. R.: Regulation of algal blooms in Antarctic shelf waters by the
1473 release of iron from melting sea ice, Geophys. Reseach Lett., 24(20), 2515–2518, 1997.

1474 Sedwick, P. N., DiTullio, G. R. and Mackey, D. J.: Iron and manganese in the Ross Sea,
1475 Antarctica: Seasonal iron limitation in Antarctic shelf waters, J. Geophys. Res., 105(C5), 11321–
1476 11336, 2000.

1477 Sedwick, P. N., Marsay, C. M., Sohst, B. M., Aguilar-Islas, A. M., Lohan, M. C., Long, M. C.,
1478 Arrigo, K. R., Dunbar, R. B., Saito, M. A., Smith, W. O. and DiTullio, G. R.: Early season
1479 depletion of dissolved iron in the Ross Sea polynya: Implications for iron dynamics on the
1480 Antarctic continental shelf, J. Geophys. Res., 116, C12019, doi:10.1029/2010JC006553, 2011.

1481 Smetacek, V., Klaas, C., Strass, V. H., Assmy, P., Montresor, M., Cisewski, B., Savoye, N.,
1482 Webb, A., D'Ovidio, F., Arrieta, J. M., Bathmann, U., Bellerby, R., Berg, G. M., Croot, P.,
1483 Gonzalez, S., Henjes, J., Herndl, G. J., Hoffmann, L. J., Leach, H., Losch, M., Mills, M. M.,
1484 Neill, C., Peeken, I., Röttgers, R., Sachs, O., Sauter, E., Schmidt, M. M., Schwarz, J.,
1485 Terbrüggen, A. and Wolf-Gladrow, D.: Deep carbon export from a Southern Ocean iron-
1486 fertilized diatom bloom, Nature, 487, 313–319, doi:10.1038/nature11229, 2012.

1487 Smith, W. O. J. and Jones, R. M.: Vertical mixing, critical depths, and phytoplankton growth in
1488 the Ross Sea, ICES J. Mar. Sci., 72(6), 1952–1960, 2015.

1489 Spackeen, J. L., Sipler, R. E., Bertrand, E. M., Xu, K., McQuaid, J. B., Walworth, N. G.,
1490 Hutchins, D. A., Allen, A. E. and Bronk, D. A.: Impact of temperature, CO2, and iron on nutrient
1491 uptake by a late-season microbial community from the Ross Sea, Antarctica, Aquat. Microb.
1492 Ecol., 82, 145–159, doi:10.3354/ame01886, 2018.

1493 St-Laurent, P., Yager, P. L., Sherrell, R. M., Stammerjohn, S. E. and Dinniman, M. S.: Pathways
1494 and supply of dissolved iron in the Amundsen Sea (Antarctica), J. Geophys. Res. Ocean., 122(9),
1495 7135–7162, doi:10.1002/2017JC013162.Received, 2017.

1496 Sunda, W. G.: Trace metal interactions with marine phytoplankton, Biol. Oceanogr., 6(5–6),
1497 411–442, doi:10.1080/01965581.1988.10749543, 1989.

1498 Sunda, W. G.: Feedback interactions between trace metal nutrients and phytoplankton in the
1499 ocean, Front. Microbiol., 3, 204, doi:10.3389/fmicb.2012.00204, 2012.

1500 Sunda, W. G. and Huntsman, S. A.: Regulation of cellular manganese and manganese transport
1501 in the unicellular rates alga Chlamydomonas, Limnol. Oceanogr., 30(1), 71–80,
1502 doi:10.4319/lo.1985.30.1.0071, 1985.

1503 Sunda, W. G. and Huntsman, S. A.: Feedback interactions between zinc and phytoplankton in
1504 seawater, Limnol. Oceanogr., 37(1), 25–40, doi:10.4319/lo.1992.37.1.0025, 1992.

1505 Sunda, W. G. and Huntsman, S. A.: Cobalt and zinc interreplacement in marine phytoplankton:
1506 Biological and geochemical implications, Limnol. Oceanogr., 40(8), 1404–1417,
1507 doi:10.4319/lo.1995.40.8.1404, 1995.

1508 Sunda, W. G. and Huntsman, S. A.: Antagonisms between cadmium and zinc toxicity and
1509 manganese limitation in a coastal diatom, Limnol. Oceanogr., 41(3), 373–387, 1996.

1510 Sunda, W. G. and Huntsman, S. A.: Effect of Zn, Mn, and Fe on Cd accumulation in
1511 phytoplankton: Implications for oceanic Cd cycling, Limnol. Oceanogr., 45(7), 1501–1516,
1512 2000.

1513 Taylor, G. T. and Sullivan, C. W.: Vitamin B12 and cobalt cycling among diatoms and bacteria
1514 in Antarctic sea ice microbial communities, Limnol. Oceanogr., 53(5), 1862–1877, 2008.

1515 Warren, M. J., Raux, E., Schubert, H. L. and Escalante-Semerena, J. C.: The biosynthesis of
1516 adenosylcobalamin (vitamin B12), Nat. Prod. Rep., 19, 390–412, doi:10.1039/B108967F, 2002.

1517 Westerlund, S. and Öhman, P.: Cadmium, copper, cobalt, nickel, lead, and zinc in the water
1518 column of the Weddell Sea, Antarctica, Geochim. Cosmochim. Acta, 55(8), 2127–2146,
1519 doi:10.1016/0016-7037(91)90092-J, 1991.

1520 Zhu, Z., Xu, K., Fu, F., Spackeen, J. L., Bronk, D. A. and Hutchins, D. A.: A comparative study
1521 of iron and temperature interactive effects on diatoms and Phaeocystis antarctica from the Ross
1522 Sea, Antarctica, Mar. Ecol. Prog. Ser., 550, 39–51, doi:10.3354/meps11732, 2016.